A scale-dependent analysis of the barotropic vorticity budget in a global ocean simulation

Hemant Khatri[1,2*], Stephen M. Griffies[2,3], Benjamin A. Storer[4], Michele Buzzicotti[5], Hussein Aluie[4,6], Maike Sonnewald[2,3], Raphael Dussin[3], Andrew Shao[7]

[1]Department of Earth, Ocean and Ecological Sciences, University of Liverpool, UK
[2]Atmospheric and Oceanic Sciences Program, Princeton University, USA
[3]NOAA Geophysical Fluid Dynamics Laboratory, Princeton, USA
[4]Department of Mechanical Engineering, University of Rochester, USA
[5]Department of Physics and INFN, University of Rome Tor Vergata, Italy
[6]Laboratory for Laser Energetics, University of Rochester, USA
[7]Canadian Centre for Climate Modelling and Analysis, Victoria, British Columbia, Canada

Key Points:

- Relative magnitudes of barotropic vorticity budget terms display significant regional variability and length-scale dependence.
- Bottom pressure torque and wind stress curl control the depth-integrated meridional flow at length scales larger than 10° (roughly 1000 km).
- Nonlinear advection and bottom pressure torque dominate the vorticity budget at smaller length scales.

*111, Nicholson Building, University of Liverpool, Liverpool L3 5DA, UK

Corresponding author: Hemant Khatri, `hkhatri@liverpool.ac.uk`

Abstract

The climatological mean barotropic vorticity budget is analyzed to investigate the relative importance of surface wind stress, topography and nonlinear advection in dynamical balances in a global ocean simulation. In addition to a pronounced regional variability in vorticity balances, the relative magnitudes of vorticity budget terms strongly depend on the length-scale of interest. To carry out a length-scale dependent vorticity analysis in different ocean basins, vorticity budget terms are spatially filtered by employing the coarse-graining technique. At length-scales greater than 10° (or roughly 1000 km), the dynamics closely follow the Topographic-Sverdrup balance in which bottom pressure torque, surface wind stress curl and planetary vorticity advection terms are in balance. In contrast, when including all length-scales resolved by the model, bottom pressure torque and nonlinear advection terms dominate the vorticity budget (Topographic-Nonlinear balance), which suggests a prominent role of oceanic eddies, which are of $\mathcal{O}(10-100)$ km in size, and the associated bottom pressure anomalies in local vorticity balances at length-scales smaller than 1000 km. Overall, there is a transition from the Topographic-Nonlinear regime at scales smaller than 10° to the Topographic-Sverdrup regime at length-scales greater than 10°. These dynamical balances hold across all ocean basins; however, interpretations of the dominant vorticity balances depend on the level of spatial filtering or the effective model resolution. On the other hand, the contribution of bottom and lateral friction terms in the barotropic vorticity budget remains small and is significant only near sea-land boundaries, where bottom stress and horizontal friction generally peak.

Plain Language Summary

Vorticity provides a measure of the local circulation of fluid flow. The analysis of physical processes contributing to ocean vorticity has proven fundamental to our understanding of how those processes drive ocean flows, ranging from large-scale ocean gyres to a few km-scale boundary currents such as the Gulf Stream. Furthermore, a vorticity analysis can inform us about the relative importance of different physical processes in generating flow structures having different length scales. In the present work, we perform a length-scale dependent vorticity budget analysis using the coarse-graining method to filter out signals larger than a fixed length scale. We coarse-grain the climatological mean vorticity budget terms over a range of length scales, and then compare the relative magnitudes to identify the dominant vorticity balances as a function of length scale.

We find that the spatial structure of the meridional transport is mainly controlled by atmospheric winds, bathymetry and nonlinear advection. However, the relative magnitudes of these factors change drastically at different length scales. We conclude that physical interpretations of the primary vorticity balances are fundamentally dependent on the chosen length scale of the analysis.

1 Introduction

Vorticity budget analyses are quite effective for understanding how surface winds drive ocean motions at different length scales. In particular, the classical Stommel model of the wind-driven gyre has provided significant insight into how surface wind stress spins up ocean gyres according to the steady balance (Stommel, 1948; Munk, 1950),

$$\rho_o \, \beta \, V = \hat{\boldsymbol{z}} \cdot \left(\nabla \wedge \boldsymbol{\tau}_{\mathrm{s}} - \nabla \wedge \boldsymbol{\tau}_{\mathrm{b}} \right). \tag{1}$$

Equation (1) shows that the vertical component of the surface wind stress curl, $\hat{\boldsymbol{z}} \cdot (\nabla \wedge \boldsymbol{\tau}_{\mathrm{s}})$, balances a meridional flow (V is the vertically-integrated meridional velocity) through the $\beta-$effect, which is commonly known as "Sverdrup balance" (Sverdrup, 1947). Also, the mass conservation condition requires a return meridional flow, which appears to be controlled by bottom friction stress, $\hat{\boldsymbol{z}} \cdot (\nabla \wedge \boldsymbol{\tau}_{\mathrm{b}})$. The Stommel model effectively explained the east-west asymmetry due to nonzero β and flow intensification at the western boundary in the gyre circulation. In a slight modification, Munk (1950) argued that the ocean flow does not reach the ocean bottom so that horizontal friction acts mainly along the western boundary; thus, permitting a return flow along the western boundary.

The Stommel and Munk models apply to a flat bottom ocean since neither model accounts for bathymetry. If we take the curl of depth-integrated momentum equations to derive a linear vorticity equation in the presence of a variable topography at $z = -H(x, y)$, the resulting vorticity equation has an additional term known as the bottom pressure torque (Holland, 1973; Hughes & De Cuevas, 2001),

$$\rho_o \, \beta \, V = \hat{\boldsymbol{z}} \cdot \left(\nabla \wedge \boldsymbol{\tau}_{\mathrm{s}} - \nabla \wedge \boldsymbol{\tau}_{\mathrm{b}} \right) + J(p_{\mathrm{b}}, H). \tag{2}$$

A nonzero bottom pressure torque, $J(p_{\mathrm{b}}, H) = \hat{\boldsymbol{z}} \cdot (\nabla p_{\mathrm{b}} \wedge \nabla H)$, arises due to varying bottom pressure along isobath contours, and the variations in bottom pressure, p_{b}, exert a nonzero torque on fluid lying over a variable topography (Jackson et al., 2006). In essence, equation (2) implies that the return flow along the western boundary can be balanced by bottom pressure torque, and western boundary currents can be perceived as being largely inviscid because friction is not required to explain a closed gyre circulation (Hughes, 2000; Hughes & De Cuevas, 2001). In fact, Schoonover et al. (2016) carried out vorticity budget analysis in realistic simulations from three different ocean models and found that bottom pressure torque controls the Gulf Stream flow magnitude along the western boundary; thus, the Gulf Stream is indeed largely inviscid (also see Gula et al., 2015; Le Bras et al., 2019). The three-way balance among $\rho_o \beta V$, bottom pressure torque, and surface wind stress curl is called "Topographic-Sverdrup balance" (Holland, 1967). Notably, friction is ultimately necessary for energy conservation and maintaining a steady state in the presence of wind forcing since bottom pressure torque does not dissipate energy (Jackson et al., 2006). However, in the presence of realistic bottom pressure torques, the role of friction (either bottom or side friction) for establishing basin-scale gyre circulations is no longer fundamental.

Several works have shown that bottom pressure torque appears as a first-order term in the vorticity budget of the depth-integrated flow and is crucial for understanding the returning boundary flows in gyres (Hughes & De Cuevas, 2001; Le Bras et al., 2019; Lu & Stammer, 2004; Sonnewald et al., 2019; Yeager, 2015). However, there remains significant regional variability in the relative magnitudes of vorticity budget terms. For example, in the North Atlantic Ocean, wind stress curl tends to be more important in controlling the depth-integrated meridional flow in the subtropics (except along the western boundary), whereas bottom pressure torque balances $\rho_o \beta V$ in almost all of the subpolar basin (Le Bras et al., 2019; Sonnewald & Lguensat, 2021; Yeager, 2015). Global analyses from ocean state estimates and in situ observations also show that the Sverdrup-balance holds only in the tropics and subtropics (Gray & Riser, 2014; Thomas et al., 2014; Wunsch, 2011). This regional variability in the relative importance of wind stress curl and bottom pressure torque arises partly due to the nature of bottom pressure torque, which vanishes when integrated along an isobath. Hence, bottom pressure anomalies can lead to non-local effects and induce meridional flows in regions having no local surface forcing via wind stress curl in the vorticity budget (Stewart et al., 2021). Consequently, it is important to consider regional differences in vorticity budget terms.

In addition to the regional variability, spatial resolution in an ocean model affects the interpretation of dominant vorticity balances. In general, Stommel-type vorticity models (equations 1 and 2) apply to large-scale ocean flows. Thomas et al. (2014) showed that a linear Sverdrup balance only holds at length scales greater than 5° in ocean models. At relatively small length scales, i.e., mesoscales and submesoscales, ocean eddies and the associated nonlinearities make a notable contribution to the vorticity budget. Using an eddy-resolving simulation of the North Atlantic Ocean, Le Corre et al. (2020) showed that bottom pressure torque and curl of nonlinear advection terms (see equation 3) appear to be the largest vorticity budget terms. On the other hand, Yeager (2015) performed vorticity analysis in a non-eddy-resolving ocean simulation and observed that the nonlinear advection term had an insignificant contribution to the overall vorticity budget, and the meridional flow was mainly controlled by bottom pressure torque and surface wind stress. Thus, interpretations of vorticity analyses depend on the region of interest, as well as the length scale of interest.

Several model-based vorticity analyses have shown that spatial resolution and the details of the topographic variations are crucial for examining the relative magnitudes of vorticity budget terms (e.g. Hughes & De Cuevas, 2001; Le Corre et al., 2020; Yeager, 2015). However, a quantitative comparison is not feasible because these studies used different ocean models that significantly differ in terms of numerical methods, sub-grid parameterizations, and other features, each of which can affect the magnitudes of the vorticity terms (Styles et al., 2022). The present study investigates the primary balances in the vorticity budget of the depth-integrated flow in an eddy-permitting global ocean simulation and quantifies the impacts of spatial resolution on dynamical balances. In addition to analyzing the regional variability in vorticity budget terms, we examine how the relative magnitudes of these terms change as a function of length scale, which is achieved by employing the coarse-graining technique (Buzzicotti et al., 2023; Storer et al., 2022). In particular, spatial maps of vorticity budget terms are examined at different filtering length-scales to understand the relative contributions of different processes in controlling the magnitude of the βV term. The methodology is described in section 2, and the results are in section 3. Conclusions and broader implications of this study are discussed in section 4.

We offer four appendices that detail the methods used to perform a vorticity budget analysis and coarse-grain filter terms in that budget. Appendix A presents the mathematical expressions for the vorticity of the depth integrated flow; Appendix B details the budget terms saved online in MOM6 ocean model and how we then compute the vorticity terms offline; and Appendix C discusses the magnitudes of the vorticity budget terms. Finally, Appendix D compares results from the coarse-graining method to the spatial filtering algorithm of Grooms et al. (2021), revealing that the two approaches agree qualitatively.

2 Methodology

2.1 Theory of Vorticity Budget Analysis

We analyze the vorticity budget based on the depth-integrated Boussinesq-hydrostatic ocean primitive equations. Several studies have employed this vorticity budget approach to examine the role of surface wind stress, bottom pressure, and ocean eddies in governing the flow dynamics (e.g. Le Corre et al., 2020; Hughes & De Cuevas, 2001; Yeager, 2015), see Waldman and Giordani (2023) for a recent review. The complete vorticity budget of the depth-integrated flow can be written as (see Appendix A for derivation)

$$\beta V = \frac{J(p_{\rm b}, H)}{\rho_o} + \hat{\boldsymbol{z}}\cdot\left(\frac{\nabla\wedge\boldsymbol{\tau}_{\rm s}}{\rho_o} - \frac{\nabla\wedge\boldsymbol{\tau}_{\rm b}}{\rho_o} + \nabla\wedge\mathcal{A} + \nabla\wedge\mathcal{B}\right) - f\,\frac{Q_m}{\rho_o} + f\,\partial_t\eta - \hat{\boldsymbol{z}}\cdot(\nabla\wedge\mathcal{U}_t)\,, \quad (3)$$

where $\beta = \partial_y f$ is the meridional derivative of the Coriolis parameter, V is the vertically-integrated meridional velocity, $z = \eta$ is sea free surface height, $z = -H$ is ocean bottom, $p_{\rm b}$ is bottom pressure, $\nabla = \hat{\boldsymbol{x}}\,\partial_x + \hat{\boldsymbol{y}}\,\partial_y$, and $\rho_o = 1035$ kg m^{-3} is the Boussinesq reference density. $\boldsymbol{\tau}_{\rm s}$ and $\boldsymbol{\tau}_{\rm b}$ are surface wind stress and bottom friction stress fields, respectively. $\mathcal{A}$ and $\mathcal{B}$ represent the vertically integrated velocity advection and velocity friction terms. Q_m is the downward mass flux on the ocean surface and $\mathcal{U}_t$ is the vertically integrated velocity tendency term. By assuming a steady state, linear, and flat bottom ocean, equation (3) readily reduces to the Stommel model of wind-driven gyre given by equation (1).

It is important to note that there are other ways to derive a two-dimensional vorticity equation, e.g., compute the curl of the depth-averaged velocity equations (Mertz & Wright, 1992), the curl of the velocity equations at each depth level and then compute the vertical integral or mean. All these formulations are equally valid and can be used depending on the research problem at hand (these variations on vorticity budgets are reviewed in Waldman & Giordani, 2023). In this study, we only use the vorticity budget formulation in equation (3), which will be referred to as the "barotropic vorticity budget". We discuss our results in the context of previous studies that used the same formulation.

2.2 Diagnosing Vorticity Budget Terms in a Global Ocean Simulation

For the vorticity budget analysis, we employ output from the global ocean-sea ice model GFDL-OM4.0, which is constructed by coupling the Modular Ocean Model version 6 (MOM6)(Adcroft et al., 2019; Griffies et al., 2020) with the Sea Ice Simulator version 2 (SIS2). GFDL-OM4.0 configuration has 1/4° horizontal grid spacing, which permits mesoscale eddies especially in the lower latitudes, and uses a hybrid z^*-isopycnal vertical coordinate, which significantly reduces artificial numerical mixing and the associated biases (Adcroft et al., 2019; Tsujino et al., 2020). For the present work, GFDL-OM4.0 was forced using JRA-55 reanalysis data (Tsujino et al., 2018) following the Ocean Model Intercomparison Project protocol (Griffies et al., 2016; Tsujino et al., 2020), and the time-mean model output for 60 years (1958–2017) is used for the barotropic vorticity budget analysis.

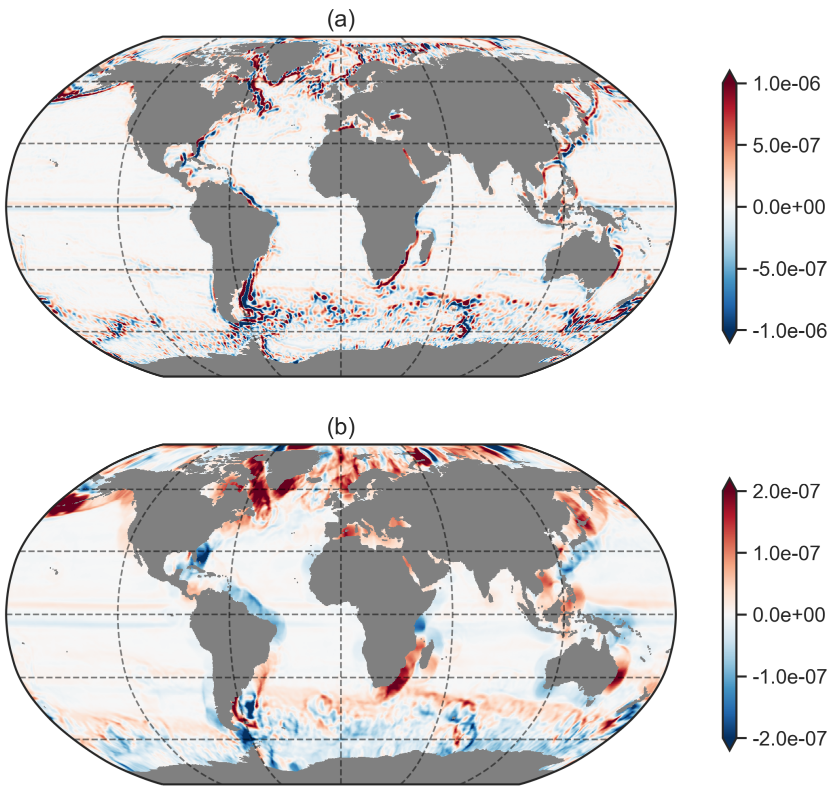

Figure 1. Spatial maps of the vertical component of relative vorticity (units are in s^{-1}) computed using the time-mean (1958–2017), depth-averaged velocity. The plotted vorticity maps are coarse-grained to (a) 2°, (b) 10° horizontal resolution (used FlowSieve package, Storer & Aluie, 2023).

Since vorticity has a higher-order spatial derivative than velocity, the vorticity field can be very noisy due to strong spatial and regional variability, which is especially enhanced at small length scales (see the maps of relative vorticity of the depth-averaged flow in Figure 1). Hence, it requires additional care to have a fully closed barotropic vorticity budget. To diagnose the vorticity budget terms in equation (3), different terms in the depth-integrated primitive velocity equations from the model are saved as diagnostics, and the curl of these diagnostics is computed to obtain the relevant barotropic vorticity budget terms (see Appendix B for details). Computing the vorticity budget terms directly from the depth-integrals of velocity equation terms reduces numerical errors due to mathematical manipulations and interpolation, and the vorticity budget closes at machine precision.

We point to the particularly difficult task of accurately computing bottom pressure torques using the Jacobian operator, $J(p_\mathrm{b}, H)$, which generally leads to significant numerical errors due to large topographic gradients. To minimize these numerical errors, bottom pressure torque can be computed as the residual of all other vorticity budget terms (Le Bras et al., 2019), or we can locally smooth bottom topography to obtain realistic magnitudes in bottom pressure torque (Le Corre et al., 2020). Our preferred method to compute bottom pressure torque is to compute the curl of vertically-integrated pressure gradient terms from the velocity equations. The same approach holds for the rest of the terms in the barotropic vorticity budget. Hence, to be consistent with the model numerical schemes and minimize the numerical errors in offline calculations, we compute vorticity budget terms directly from the depth-integrated momentum budget diagnostics.

As seen in the spatial maps of the time-mean vorticity budget terms, βV, bottom pressure torque, the nonlinear advection curl, and the surface wind stress curl dominate the barotropic vorticity budget in terms of the magnitude (Figure 2a–2d). However, there is a significant spatial variability in the relative magnitudes of the vorticity budget terms. The vorticity balance tends to be very region dependent, as different terms dominate in different geographical locations (also see Sonnewald et al., 2019; Sonnewald & Lguensat, 2021). For example, the global means of bottom friction and lateral friction stress terms are negligible (Figure 2e–2f); however, these terms have notable contributions in local balances especially near continental boundaries. These characteristics of the vorticity budget terms motivate a vorticity analysis considered separately in different ocean regions (e.g. see Le Corre et al., 2020; Palóczy et al., 2020). Note that the remainder of the vorticity budget terms, which are associated with surface mass flux and time-tendencies (Figures 2g–2i), have a negligible contribution. Even so, we include them in the analyses to enable a fully closed vorticity budget.

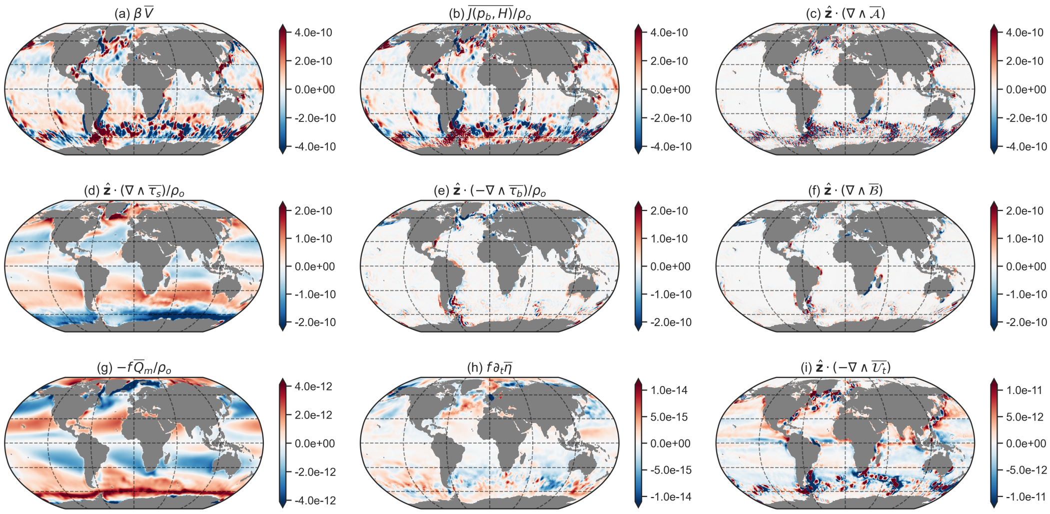

Figure 2. Time-mean (1958–2017, indicated with overbars) barotropic vorticity budget terms (units are in m s^{-2}). Each of the fields are coarse-grained to 5° spatial resolution (used FlowSieve package, Storer & Aluie, 2023). Note the different colorbar ranges on the panels.

Signs of the barotropic vorticity budget terms can rapidly change spatially (e.g., see spatial variations in bottom pressure torque and nonlinear advection term in the Southern Ocean in Figures 2a–2c). Hence, positive and negative signals tend to cancel when integrated over large domains. For example, the global averages of bottom pressure torque and nonlinear advection vanish and the main balance is between surface wind stress and friction terms. As a result, a domain-averaged vorticity budget cannot pick up fields that have large magnitudes but with spatially alternating signs. The resultant domain-averaged vorticity balance cannot represent the true nature of vorticity dynamics and can lead to incomplete or incorrect interpretations. To overcome these issues, we employ the coarse-graining technique to deduce the dominant vorticity budget terms appearing at different length scales (Buzzicotti et al., 2023). Coarse-graining allows us to examine the local and non-local impacts of different processes as a function of length scale, while maintaining the structure of the patterns corresponding to scales at or larger than the chosen coarse-graining scale. In the present work, we focus on the impacts of the choice of length scale on local barotropic vorticity balances.

2.3 The coarse-graining method

Coarse-graining can be used to examine the spatial variability in a multi-dimensional field. For any field, $F(\mathbf{x})$, the coarse-graining produces a filtered field, $F_\ell(\mathbf{x})$, that has variability only on scales longer than l (Buzzicotti et al., 2023). $F_\ell(\mathbf{x})$ is computed as

$$F_\ell(\mathbf{x}) = G_\ell * F(\mathbf{x}), \tag{4}$$

where $*$ is the convolution on the sphere (Aluie, 2019) and G_ℓ is a normalized filtering kernel, which is a top-hat filter in this study (see equation (4) in Storer et al., 2022), so that $\int_A G_\ell = 1$. Relation (4) basically represents a spatial average of $F(\mathbf{x})$ centered at geographical location $\mathbf{x}$.

In practice, the coarse-graining technique can be applied to the entire globe, which has land/sea boundaries, while preserving the fundamental physical properties, such as the global variance of a field and non-divergence of the velocity in a Boussinesq ocean (Aluie, 2019). Coarse-graining has been successfully used for analyzing the kinetic energy spectrum and inter-scale energy transfers in the oceans (Aluie et al., 2018; Rai et al., 2021; Storer et al., 2022). Since the vorticity budget term magnitudes tend to peak around continental boundaries (Figure 2), spatial filtering near boundaries requires additional care so that there are no artificial large signals as a result of the spatial filtering. The coarse-graining technique is well suited for the present analysis as it handles gradients around land-sea boundaries appropriately.

Following the steps described in section 2.2, we compute the barotropic vorticity budget diagnostics, which are then coarse-grained by employing the FlowSieve package (Storer & Aluie, 2023). Prior to coarse-graining, vorticity budget diagnostics were re-gridded to a uniform $0.25^\circ \times 0.25^\circ$ grid because the current implementation of FlowSieve package only accepts rectangular latitude-longitude grids. Since we only analyze the vertical vorticity component, the barotropic vorticity budget terms are treated as scalar fields for the purpose of coarse-graining. We use the fixed-kernel method, in which land is treated as ocean with zero vorticity, to conserve global averages of vorticity terms (Buzzicotti et al., 2023). Coarse-grained diagnostics are then analyzed to identify the dominant vorticity balances as a function of filter scale, ℓ. In particular, the spatial structure of the coarse-grained vorticity budget fields is examined for different magnitudes of the filter scale, which is expressed either in degree or km. Although setting the filter scale in km is a natural choice for preserving the global area-weighted variance, the coarse-graining filter scale in degree units is used to understand how the grid spacing in a model affects the dominant vorticity balances. The coarse-graining in degree is performed by assigning equal weights to all model grid cells whereas, for the coarse-graining in km, actual grid cell areas are used as weights. Note that, for both coarse-graining in degree and km, the point-wise vorticity budget is closed for coarse-grained vorticity terms and the global averages (when calculated with appropriate weights) of vorticity terms are conserved.

Furthermore, we compute root-mean-square magnitudes, $\sqrt{\{F_\ell^2\}}$, for all the vorticity budget terms in different ocean regions and analyze their relative magnitudes as a function of filter scale,

$$\sqrt{\{F_\ell^2\}} = \sqrt{\frac{\sum_i w_i F_\ell(\mathbf{x_i})^2}{\sum_i w_i}}, \tag{5}$$

where i is a grid cell index within a region and w_i is the associated weight. For coarse-graining in km, w_i is equal to the grid cell area, and, for coarse-graining in degree, $w_i = 1$. The root-mean-square magnitudes are used to investigate the regional variability in vorticity balances. Note that $\sqrt{\{F_\ell^2\}}$ magnitudes decline significantly with increasing the coarse-graining filter scale (see appendix Figure C1). Thus, we analyze the normalized $\sqrt{\{F_\ell^2\}}$ magnitudes as a function of filter scale to measure the relative importance of different vorticity budget terms,

$$\sqrt{\{F_\ell^2\}_j}\,(normalized) = \frac{\sqrt{\{F_\ell^2\}_j}}{\sum_j \left(\sqrt{\{F_\ell^2\}_j}\right)}, \tag{6}$$

where j corresponds to a vorticity budget term and $\sqrt{\{F_\ell^2\}_j}\,(normalized)$ measures spatial variability captured by a vorticity budget term.

3 Vorticity Budget Analysis as a Function of Length-scale

Vorticity budget analyses from relatively coarse ocean models have shown that bottom pressure torque plays a prominent role in regional vorticity balances and in guiding western boundary currents (Hughes & De Cuevas, 2001; Lu & Stammer, 2004; Yeager, 2015). On the other hand, more recent studies employed mesoscale eddy-resolving ocean models having horizontal grid spacing of $2 - 10$ km, with these studies emphasizing that bottom pressure torque and nonlinear advection are equally important for regional vorticity dynamics (Le Corre et al., 2020; Palóczy et al., 2020). The present study aims to quantify the impacts of resolution on vorticity balances using a single global ocean simulation. Coarse-grained barotropic vorticity budget terms are examined as a function of filter scale in different ocean basins to assess the impact of spatial smoothing on the magnitudes of all vorticity terms.

3.1 Vorticity Budget in the North Atlantic Ocean

At first, we examine the spatial structure of coarse-grained vorticity budget terms in the North Atlantic Ocean, which has been considered in several works (e.g. Le Corre et al., 2020; Schoonover et al., 2016; Yeager, 2015). As seen in Figure 3, all vorticity terms, except the wind stress curl, have pronounced spatial variability and peak near continental boundaries and mid-ocean topographic features.

Coarse-graining has a notable impact on the relative contributions of different vorticity terms. For example, when spatial variations larger than 2° in size are retained (Figures 3a1-3g1), βV, bottom pressure torque and the curl of the nonlinear advection term, $\nabla\wedge\mathcal{A}$, dominate in terms of the magnitude (also see Le Corre et al., 2020). Hence, the local meridional flow is controlled by bottom pressure torque and nonlinear advection (henceforth will be referred to as "Topographic-Nonlinear balance"). Surface wind stress, bottom friction, and horizontal friction terms also have large magnitudes around land-sea boundaries; however, their contribution to the local vorticity budget is relatively small. The rest of the vorticity budget terms (surface mass flux and time-tendencies) are negligible in comparison. There appears to be a significant cancellation between bottom pressure torque and $\nabla \wedge \mathcal{A}$ at mesoscales and submesoscales (smaller than about 5°), and their sum is roughly in balance with βV. Consistent with our results, Le Corre et al. (2020) found that bottom pressure torque and $\nabla \wedge \mathcal{A}$ signals generally are of opposite signs to each other, so that these two terms compensate for each other (also see Gula et al., 2015).

On the other hand, with coarse-graining at scales 10° and larger (Figures 3a3-3g3), $\nabla \wedge \mathcal{A}$ almost disappears, and the dominant balance is then among βV, bottom pressure torque and wind stress curl. This result suggests that vorticity dynamics at large scales are close to the Topographic-Sverdrup balance, which agrees with vorticity budget analyses from relatively coarse ocean models (Lu & Stammer, 2004; Yeager, 2015). The coarse-graining exercise shows that bottom pressure torque is significant at all length scales, whereas $\nabla\wedge\mathcal{A}$ contribution to the barotropic vorticity budget is limited to scales smaller than 10°. These results indicate that the model resolution (or the length scale

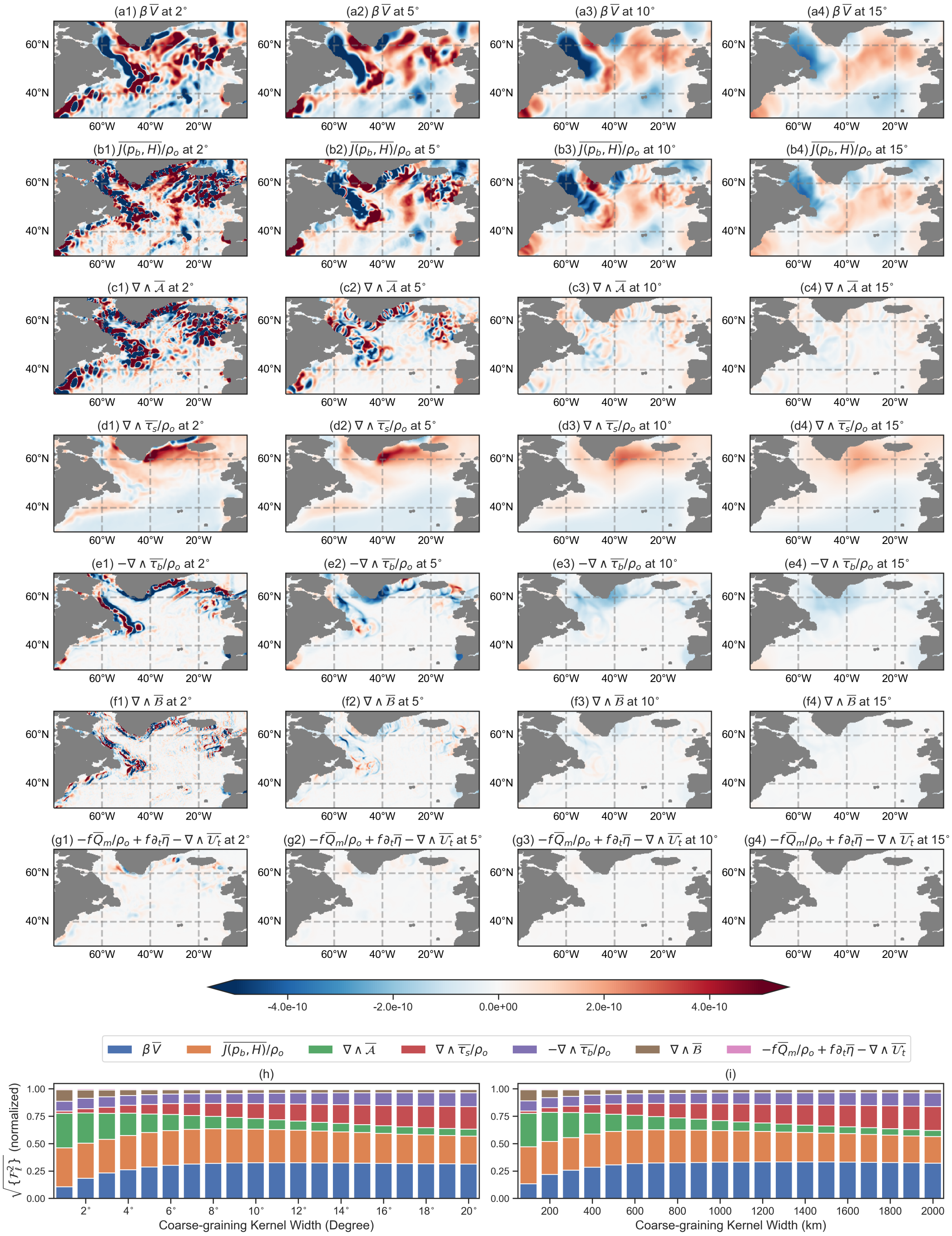

Figure 3. Vorticity budget analysis for the North Atlantic Ocean (a-g) Time-mean (1958–2017, indicated with overbars) spatial maps of barotropic vorticity budget terms (units are in m s^{-2}) as a function of the coarse-graining filter scale; (h-i) Normalized magnitudes of the root-mean-square budget terms (see equation 6) at different coarse-graining filter scales (in degree and km). $\sqrt{\{F_\ell^2\}}$ is computed for the region bounded between 30°N–70°N and 80°W–0°W. Note that $\hat{\boldsymbol{z}}\cdot$ is omitted in panel titles and legends.

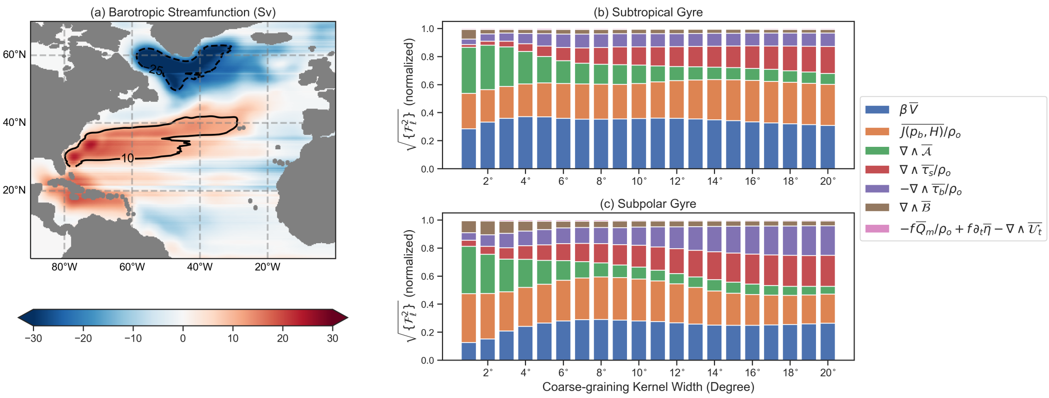

Figure 4. Vorticity budget analysis for for North Atlantic gyres (a) Time-mean (1958–2017, indicated with overbars) barotropic streamfunction computed as $\int_{x_w}^{x} \overline{V}\mathrm{d}x$; (b-c) Normalized magnitudes of the root-mean-square budget terms (see equation 6) at different coarse-graining filter scales (in degree) for the subtropical gyre (within the region of 10 Sv contour) and subpolar gyre (within the region of -25 Sv contour). For brevity, $\hat{\boldsymbol{z}}\cdot$ is omitted in the legend.

of interest) is a key parameter while examining relative contributions from different vorticity terms, as physical interpretations of these results depend on the length scale.

For a quantitative investigation on the impacts of coarse-graining on vorticity balances, we compute normalized root-mean-square values of the time-mean budget terms over the whole domain (Figure 3h). Consistent with the results discussed above, for coarse-graining with 2° filter scale (or smaller), bottom pressure torque and $\nabla\wedge\mathcal{A}$ are the largest vorticity terms and capture more than 60% of the spatial-pattern variability. βV is the third largest term and explains about 10% of the spatial-pattern variability. As the coarse-graining kernel width increases, $\nabla\wedge\mathcal{A}$ signals smooth out, and the primary balance is then among βV, bottom pressure torque, and surface wind stress curl. Together, these three terms capture more than 70% of the vorticity budget at length scales greater than 10°. The rest of the contribution to the vorticity balance is from $-\nabla\wedge\boldsymbol{\tau}_{\mathrm{b}}/\rho_o$ and $\nabla\wedge\mathcal{B}$, which project on all length scales. Overall, these vorticity analyses show a clear transition from the Topographic-Nonlinear balance to the Topographic-Sverdrup balance as we move from small to large length-scales. The conclusions remain the same if the fields are coarse-grained using kernel width in km instead of degree (Figure 3i). The contribution from $\nabla\wedge\mathcal{A}$ is minimal at length scales larger than about 1000 km. Even the coarse-grained fields obtained by setting the filter kernel in km (not shown here) are very similar to coarse-grained fields shown in Figure 3. The same results hold even if a different spatial filtering algorithm is used (see Figure D1).

3.1.1 Vorticity budget within closed gyre contours

To understand the dominant vorticity balances that control subtropical and subpolar North Atlantic gyre circulations, we analyze the root-mean-square magnitudes of vorticity budget terms within closed gyre contours (Figure 4). Even within gyres, the vorticity balance is largely among bottom pressure torque, $\nabla\wedge\mathcal{A}$, and βV when all length scales are included. When spatial features only larger than 10° are retained, there is an insignificant contribution from $\nabla \wedge \mathcal{A}$, and about 70% of the spatial-pattern variability in the barotropic vorticity terms is explained with βV, bottom pressure torque, and the surface wind stress curl. However, there is one key difference between the vorticity budgets of subtropical and subpolar gyres. At relatively large length-scales (greater than 5°), bottom friction and horizontal friction terms, $-\nabla\wedge\boldsymbol{\tau}_{\mathrm{b}}/\rho_o$ and $\nabla\wedge\mathcal{B}$, capture about 20% of the spatial-pattern variability in the subpolar gyre, whereas their contribution to the vorticity balance in the subtropical gyre is less than 10%. This difference is because a large part of the subpolar gyre is influenced by physical processes occurring near land-sea boundaries. Since bottom and horizontal friction have their peak magnitudes near continental boundaries (see Figures 3e–3f), they are more important in the vorticity budget of the subpolar gyre than in the subtropical gyre.

3.1.2 Why does the nonlinear advection term smooth out at large scales?

The nonlinear advection term mainly accounts for the redistribution of vorticity via transient eddies and standing meanders (Gula et al., 2015), which generally are 1− 300 km in size (Chelton et al., 2007; Eden, 2007). Since these nonlinear flow patterns have spatial variations over length scales smaller than about 500 km, the nonlinear term is expected to be weak at large length scales (also see Hughes & De Cuevas, 2001). To better understand this behavior, we examine the vorticity budget equation more closely. Since meridional transport is primarily controlled by bottom pressure torque and nonlinear advection at small length scales (Figures 3–4), an approximate vorticity budget

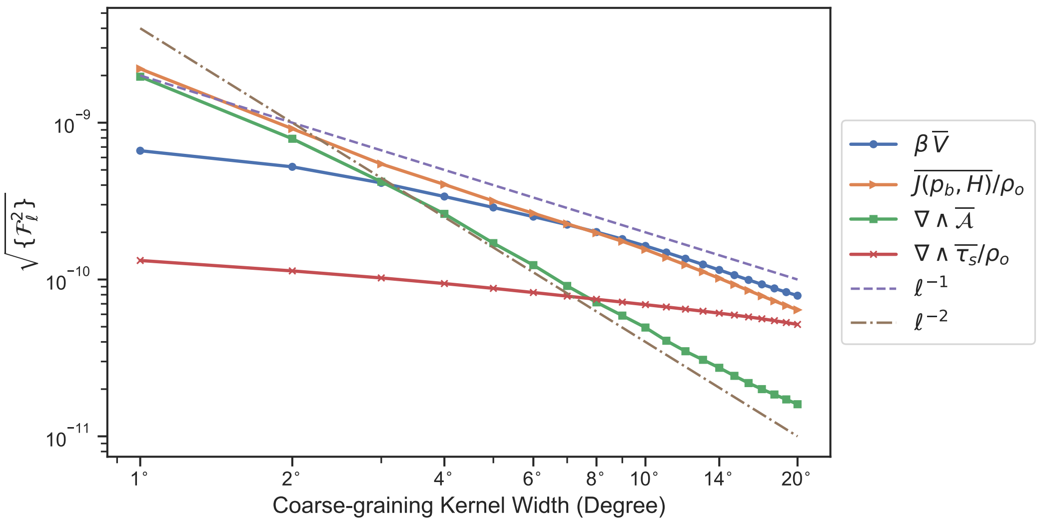

Figure 5. Scaling of the root-mean-square magnitudes, $\sqrt{\{F_\ell^2\}}$ (units are in m s^{-2}), of vorticity budget terms in the subpolar North Atlantic Ocean, region shown in Figure 3. Note that $\hat{\boldsymbol{z}}\cdot$ is omitted in the legends.

can be written as

$$\beta\, V \approx \hat{\boldsymbol{z}}\cdot\left[\frac{1}{\rho_o}\nabla\wedge(H\,\nabla p_{\rm b}) + \overbrace{\frac{1}{\rho_o}\nabla\wedge\left(\nabla\cdot\int_{-H}^{\eta}\mathbb{T}^{\rm kinetic}_{\rm hor}\,{\rm d}z\right)}^{\approx\nabla\wedge\mathcal{A}}\right], \tag{7}$$

where $\mathbb{T}^{\rm kinetic}_{\rm hor} = -\rho_o\,\mathbf{u}\otimes\mathbf{u}$ is the horizontal kinetic stress tensor whose Reynolds average leads to the Reynolds stress (see, for example, page 620 of Kundu et al., 2016). The nonlinear term is written in a different, but equivalent, form in Appendix A2. Note that there are higher-order derivatives in the nonlinear advection term and bottom pressure torque. Hence, the right-hand side terms have a stronger small-scale spatial variability and relatively larger magnitudes at small length scales than $\beta\, V$. Essentially, the nonlinear advection term and bottom pressure torque are expected to compensate for each other at small length scales, and their residual leads to a relatively large-scale structure in meridional transport (see Figures 3a1–3c1).

This qualitative argument does not provide any explanation of why the relative magnitudes of bottom pressure torque and nonlinear advection term change as a function of length scale. For further investigation, we perform a scale analysis (also see Schoonover et al., 2016),

$$\left|\frac{J(p_{\rm b}, H)}{\rho_o}\right| = |\, f\,\mathbf{u}_g\cdot\nabla H\,| \quad\approx\quad f\,\frac{\mathcal{V}\mathcal{L}_v}{\mathcal{L}_h}, \tag{8}$$

$$|\,\hat{\boldsymbol{z}} \cdot (\nabla \wedge \mathcal{A})\,| \quad \approx \quad \frac{\mathcal{V}^2 \mathcal{L}_v}{\mathcal{L}_h^2}, \tag{9}$$

where $\mathbf{u}_g$ is the horizontal geostrophic velocity at the ocean bottom, $\mathcal{V}$ is the velocity scale, $\mathcal{L}_h$ is the horizontal length scale, and $\mathcal{L}_v$ is the vertical length scale. Since $\mathcal{V}$ and $\mathcal{L}_v$ vary little with changing $\mathcal{L}_h$, equations (8)–(9) imply that the magnitudes of bottom pressure torque and the nonlinear advection term follow $1/\mathcal{L}_h$ and $1/\mathcal{L}_h^2$ scalings, respectively. Hence, the nonlinear advection term must decay faster than bottom pressure torque when increasing the horizontal length scale. At relatively large length scales, the meridional flow then has to be controlled by a combination of bottom pressure torque and surface wind stress, which each can have spatial variations on scales of atmospheric motions. As seen in Figure 5, the root-mean-square values of vorticity budget terms are in agreement with these scaling arguments. The nonlinear term roughly follows ℓ^{-2} scaling whereas the bottom pressure torque magnitude declines as ℓ^{-1}. At relatively large scales, βV dominates over $\nabla \wedge \mathcal{A}$ and the cross-over occurs near $\ell = 3°$ scale (roughly 300 km), which interestingly correlates with the mesoscale spectral peak in the global kinetic energy spectrum (Storer et al., 2022). Using the scale analysis, we estimate this cross-over length scale,

$$|\,\beta V\,| \quad \approx \quad |\,\hat{\boldsymbol{z}} \cdot (\nabla \wedge \mathcal{A})\,|, \tag{10}$$

$$\beta\, \mathcal{V} \mathcal{L}_v \quad \approx \quad \frac{\mathcal{V}^2 \mathcal{L}_v}{\mathcal{L}_h^2}. \tag{11}$$

By setting $\beta = 10^{-11}$ m^{-1}s^{-1} and $\mathcal{V} = 0.1$ m s^{-1}, we obtain $\mathcal{L}_h = 100$ km, which largely agrees with the results from Figure 5. Thus, the contribution of the nonlinear advection term to the barotropic vorticity budget can be neglected at scales larger than 300–400 km, which was also argued by Hughes and De Cuevas (2001). One caveat to note is that our analyses use output from a 0.25° ocean model, which does not resolve all mesoscale activity. Hence, the contribution of the nonlinear advection term to barotropic vorticity budget, especially at mesoscales, is not fully captured.

3.2 Vorticity Budget in Weddell Sea Region

Topography plays a fundamental role in the Southern Ocean, which comprises highly energetic ocean regions, e.g. Weddell Sea and Drake Passage, in terms of flow-topography interactions and mesoscale eddy dynamics (Hughes, 2005; Rintoul et al., 2001; Rintoul & Naveira Garabato, 2013; Rintoul, 2018). To investigate the roles of topography and nonlinear eddies on local vorticity balances, we repeat the vorticity budget analysis in

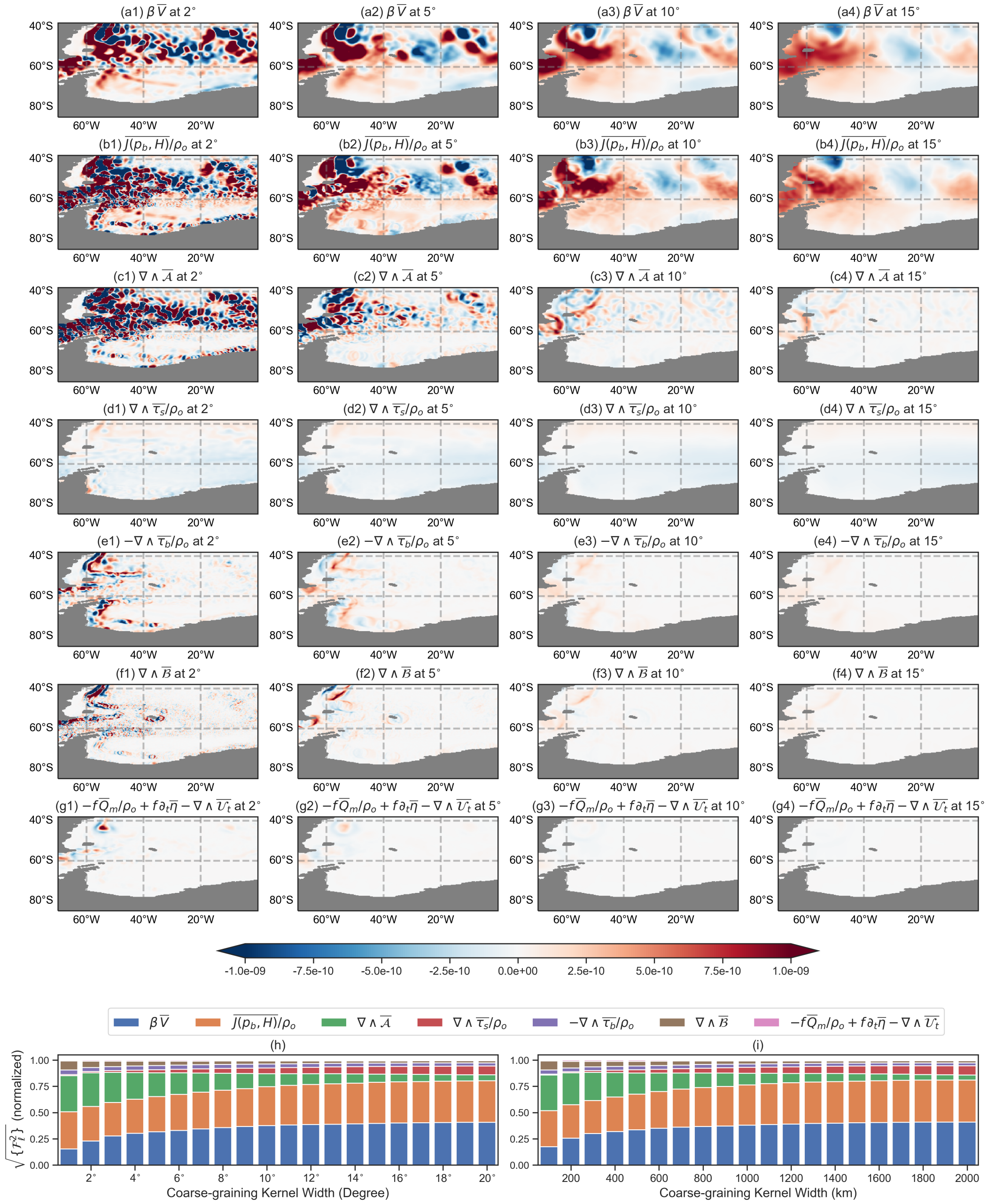

Figure 6. Vorticity budget analysis for the Weddell Sea region (a-g) Time-mean (1958–2017, indicated with overbar) spatial maps of barotropic vorticity budget terms (units are in m s^{-2}) as a function of the coarse-graining filter scale; (h-i) Normalized magnitudes of the root-mean-square budget terms (see equation 6) at different coarse-graining filter scales (in degree and km). $\sqrt{\{F_\ell^2\}}$ is computed for the region bounded between 85°S–40°S and 70°W–0°W. Note that $\hat{\boldsymbol{z}}\cdot$ is omitted in panel titles and legends.

the Weddell Sea region (Figure 6). For coarse-graining scale of $1^\circ - 2^\circ$, the main balance is among bottom pressure torque, $\nabla\wedge\mathcal{A}$, and βV. For coarse-grained fields at scales larger than about 10° (or 1000 km), the contribution from the nonlinear advection term is minimal, and βV and bottom pressure torque terms explain more than 70% of the spatial-pattern variability in the barotropic vorticity balances.

Interestingly, the relative contribution of the surface wind stress curl to the vorticity budget at length scales larger than 10° is much smaller than observed in the North Atlantic Ocean (compare Figures 3h and 6h). This behavior is because the magnitudes of βV and bottom pressure torque are much larger in the Southern Ocean than in the North Atlantic (Figures 2a–2b), whereas the wind stress curl magnitudes vary little with latitude (Figure 2d). These results do not imply that the wind component is unimportant in the Weddell Sea region. On the contrary, surface winds are a key driving force for ocean flows at all length scales. However, for the local vorticity budget and spatial variability in vorticity terms, bottom pressure torque appears to be the primary factor in governing the spatial structure of the depth-integrated meridional flow in the Weddell Sea.

3.3 Vorticity Budget in the Equatorial Pacific Ocean

The equatorial Pacific Ocean slightly differs from ocean regions at high latitudes in terms of barotropic vorticity dynamics. Here, the contribution of the nonlinear advection term to the barotropic vorticity budget is relatively small at all length scales (Figure 7). Instead, bottom pressure torque and wind stress curl are the dominant terms that balance βV at all length scales, and these three terms capture more than 80% of the spatial-pattern variability. Hence, dynamics in the equatorial Pacific Ocean largely follow the Topographic-Sverdrup balance. These results are in contrast to North Atlantic and Weddell Sea analyses, which indicate significant nonlinear eddy advection contribution to vorticity dynamics at length scales smaller than 10°.

3.4 Global Vorticity Budget

To have an understanding of the global picture of vorticity balances, we divide the global ocean into four regions and repeat the vorticity analysis in these four regions (Figure 8). These basins are sufficiently large such that the regional variability (as in sec-

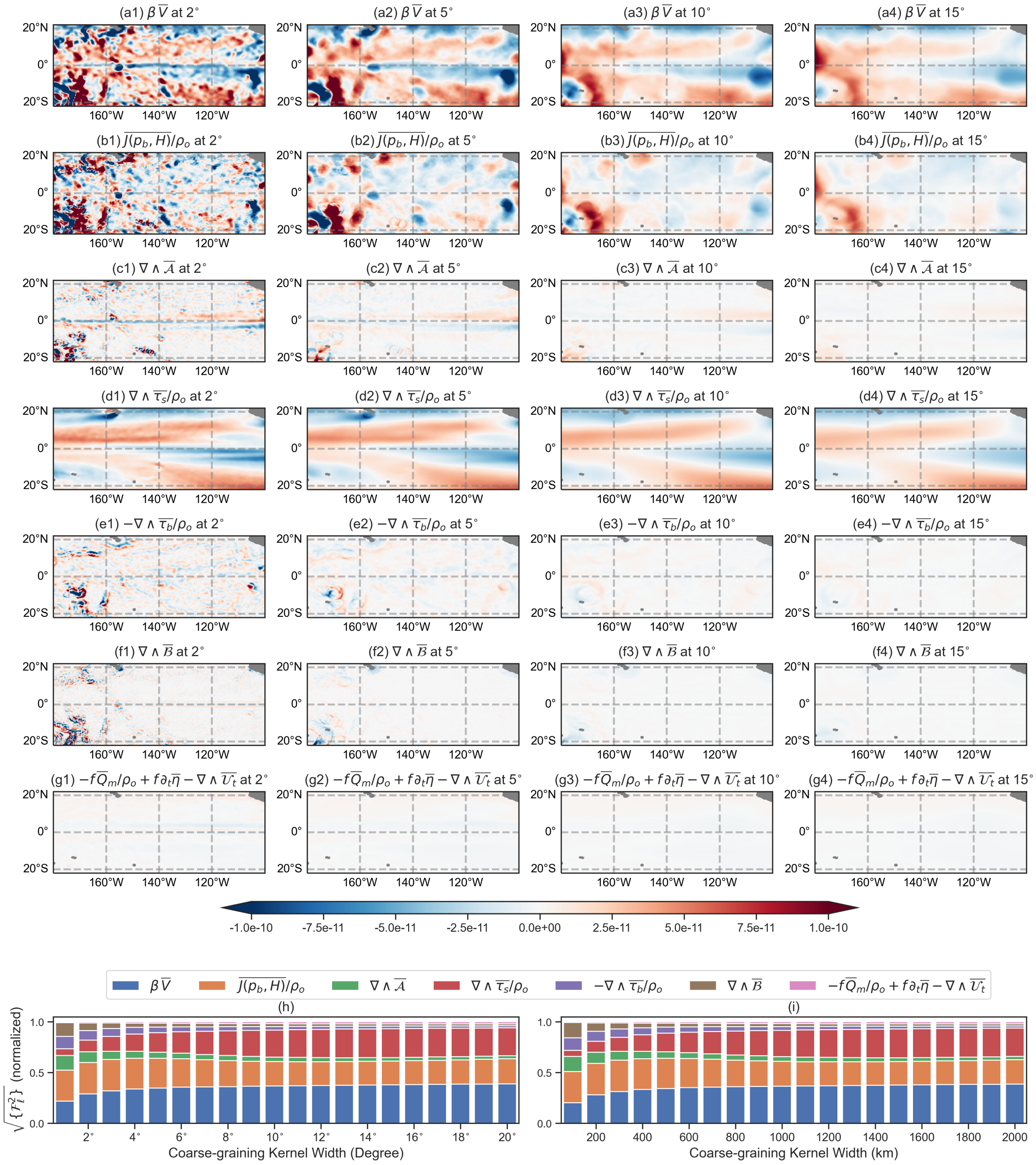

Figure 7. Vorticity budget analysis for an oceanic region in the equatorial Pacific (a-g) Time-mean (1958–2017, indicated with overbar) spatial maps of barotropic vorticity budget terms (units are in m s^{-2}) as a function of the coarse-graining filter scale; (h-i) Normalized magnitudes of the root-mean-square budget terms (see equation 6) at different coarse-graining filter scales (in degree and km). $\sqrt{\{F_\ell^2\}}$ is computed for the region bounded between 20°S–20°N and 180°W–100°W. Note that $\hat{\boldsymbol{z}}\cdot$ is omitted in panel titles and legends.

tions 3.1–3.3) becomes less apparent. In general, bottom pressure torque and βV terms are the largest terms, followed by the surface wind stress curl that appears on relatively large scales. These three terms together capture roughly 70% of the variability in spatial patterns. As seen in sections 3.1–3.3, the nonlinear advection term is only important at length scales smaller than about 10°, except in the Indian Ocean sector where, even at length scales of $10° - 20°$, the nonlinear advection term is as important as surface wind stress curl and bottom pressure torque. The relatively large contribution of the nonlinear advection in the Indian Ocean could be due to larger mesoscale eddy length scales in tropics than at higher latitudes (Chelton et al., 2007, 2011). In addition, bottom friction and horizontal friction explain about 10%–20% of the spatial pattern variations in the vorticity balance.

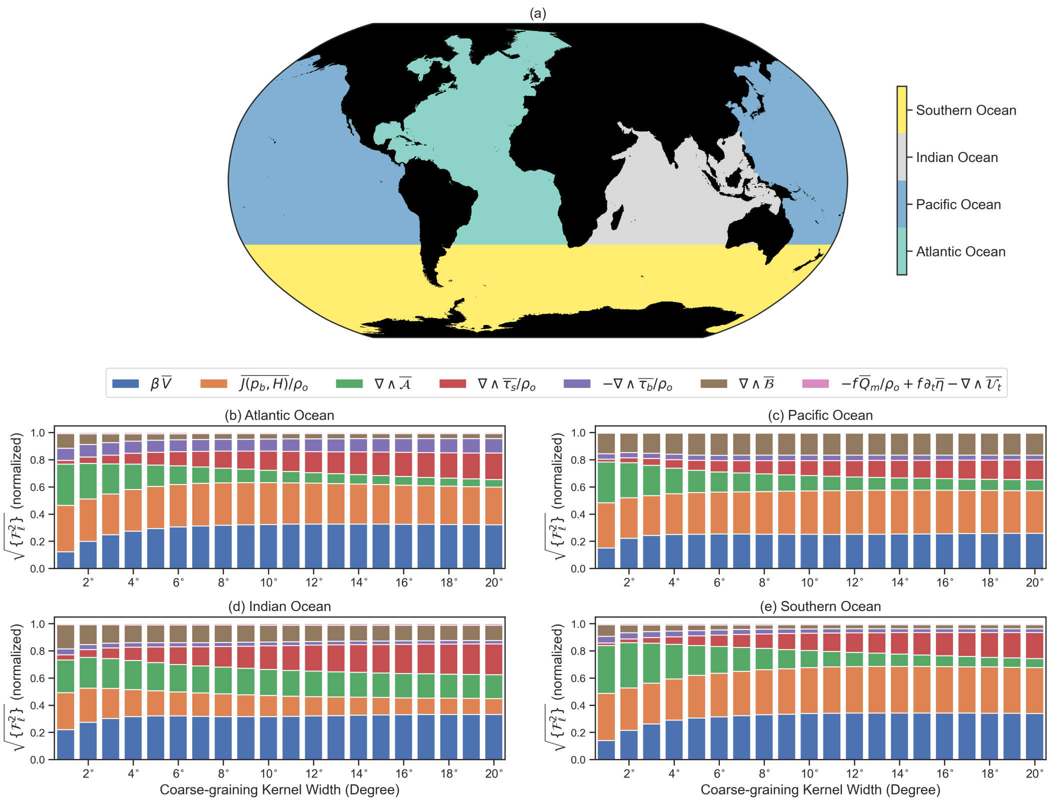

Figure 8. Vorticity budget analysis for the global ocean (a) Extent of four ocean basins (b-e) Normalized magnitudes of the root-mean-square budget terms (see equation 6) at different coarse-graining filter scales (in degree). $\sqrt{\{F_\ell^2\}}$ is computed separately for the basins shown with different colors in (a). Note that $\hat{\boldsymbol{z}}\cdot$ is omitted in the legends.

To further emphasize how spatial smoothing affects the local vorticity balance, we identify grid points at which 80% of the variability in the barotropic vorticity budget can be explained with two or three largest vorticity terms. Sonnewald et al. (2019) applied a machine learning algorithm to ECCO global ocean state estimate, which has horizontal grid spacing of 1°, and identified different dynamical regimes using the barotropic vorticity budget framework. However, impacts of the spatial resolution on these dynamical regimes have not been examined before. Here, we analyze point-wise vorticity balances for four coarse-graining filter scales (Figure 9). Firstly, three vorticity balances stand out, i.e., Topographic-Sverdrup balance, Topographic-Nonlinear balance, and Sverdrup balance. The proportion of grid points at which these balances are satisfied increases when we increase the filter length scale (see Table 1). In fact, a large part of the global ocean transitions from a Topographic-Nonlinear regime to a Topographic-Sverdrup regime, especially in the Southern Ocean. As the coarse-graining kernel width increases and more length scales are filtered out, the contribution of the nonlinear advection term decreases. In the case of 2° filter scale, the vorticity dynamics closely follow Topographic-Sverdrup and Topographic-nonlinear relationships at about 20% and 18% of the total grid points, respectively. On the other hand, these percentages change to 38% and 7%, respectively, at length scales greater than 20°.

In tropical and subtropical oceans (roughly 40°S–40°N), Sverdrup balance holds reasonably well at length scales larger than 10° (Figure 9c), which is in agreement with Gray and Riser (2014); Thomas et al. (2014); Wunsch (2011). However, Sverdrup balance rarely holds at higher latitudes in those regions where topography significantly affects the spatial variability of the depth-integrated meridional flow at large scales. This role for topography is enhanced in such regions due to a relatively weak stratification allowing for strong deep flows. Note that maps of Sverdrup and Topographic-Sverdrup relationships in Figure 9 are not mutually exclusive. If the local vorticity dynamics can be approximated as being in Sverdrup balance, then the dynamics would also be in accord with Topographic-Sverdrup balance. Hence, Sverdrup balance is a special case of Topographic-Sverdrup balance. At length scales larger than 10°, the barotropic vorticity dynamics can be understood in terms of Topographic-Sverdrup balance in more than 60% of the global ocean. A schematic of different dynamical regimes in the global ocean is shown in Figure 10.

Intriguingly, there is virtually no ocean region in the friction-dominated regime, in which βV is controlled by bottom friction and horizontal friction. This result suggests that the global ocean is dominated by inviscid processes in terms of barotropic vorticity dynamics. Indeed, there is a large part of the oceans where these simplified vorticity relationships (Topographic-Nonlinear and Topographic-Sverdrup) do not hold and vorticity dynamics are controlled by more than three terms.

	2° Kernel	5° Kernel	10° Kernel	20° Kernel
$\beta \overline{V} \approx \overline{J(p_\mathrm{b}, H)}/\rho_o + \hat{\boldsymbol{z}} \cdot (\nabla \wedge \overline{\boldsymbol{\tau}_\mathrm{s}})/\rho_o$	19.98%	31.81%	37.07%	38.01%
$\beta \overline{V} \approx \overline{J(p_\mathrm{b}, H)}/\rho_o + \hat{\boldsymbol{z}} \cdot \left(\nabla \wedge \overline{\mathcal{A}}\right)$	18.15%	14.61%	11.02%	6.80%
$\beta \overline{V} \approx \hat{\boldsymbol{z}} \cdot (\nabla \wedge \overline{\boldsymbol{\tau}_\mathrm{s}})/\rho_o$	4.99%	14.49%	20.46%	24.32%
$\beta \overline{V} \approx \hat{\boldsymbol{z}} \cdot \left(-\nabla \wedge \overline{\boldsymbol{\tau}_\mathrm{b}}/\rho_o + \nabla \wedge \overline{\mathcal{B}}\right)$	0.19%	0.06%	0.04%	0.01%
Other	56.75%	39.03%	31.41%	30.85%

Table 1. Percentage of grid points at which vorticity balances plotted in Figure 9 satisfy and capture more than 80% spatial pattern variations in vorticity balances.

4 Discussion and Conclusions

The vorticity budget of the depth-integrated flow is analyzed to understand how bottom pressure torque, surface wind stress curl, nonlinear advection, and friction drive spatial variability in meridional transport in the oceans. Previous studies have shown that interpretations of vorticity budget analyses can significantly change depending on the region of interest and length scale. For example, the classical Sverdrup balance only holds in tropics and subtropics at length scales greater than about 5° (Thomas et al., 2014; Wunsch, 2011). At higher latitudes and in eddy-active regions, barotropic pressure torque and nonlinear advection control the spatial variability in the depth-integrated meridional flow (Hughes & De Cuevas, 2001; Le Corre et al., 2020; Lu & Stammer, 2004; Yeager, 2015).

The present work investigates the regional variability and length-scale dependence in vorticity budget analyses using the 60-year mean vorticity budget terms from an eddy-permitting global ocean simulation (Adcroft et al., 2019). The time-mean vorticity bud-

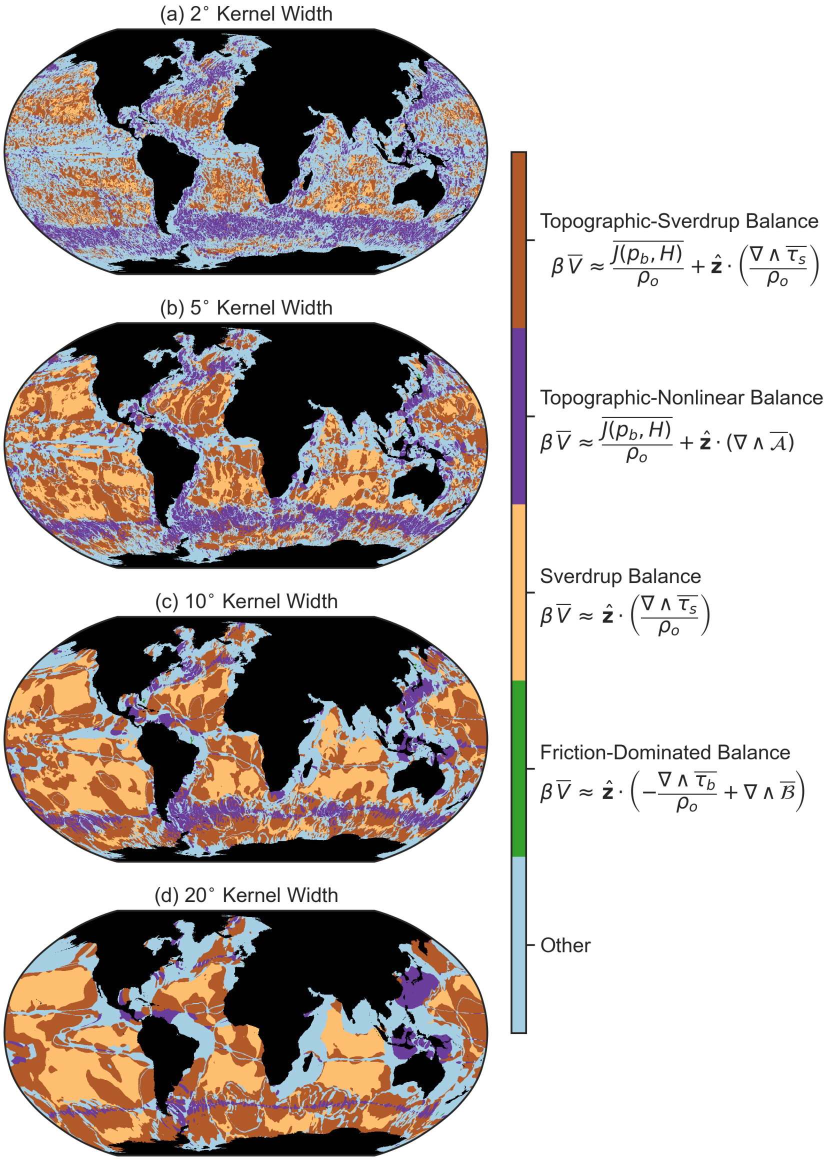

Figure 9. Global map of leading vorticity balances with different levels of coarse-graining (a) 2° kernel width (b) 5° kernel width (c) 10° kernel width (d) 20° kernel width. Different colors indicate balance among different vorticity terms (see legend), which capture 80% of the variability in the vorticity budget at any grid point. For legend 'Other', vorticity balance is complex, and more than three terms are required to capture 80% spatial-pattern variations in vorticity balances.

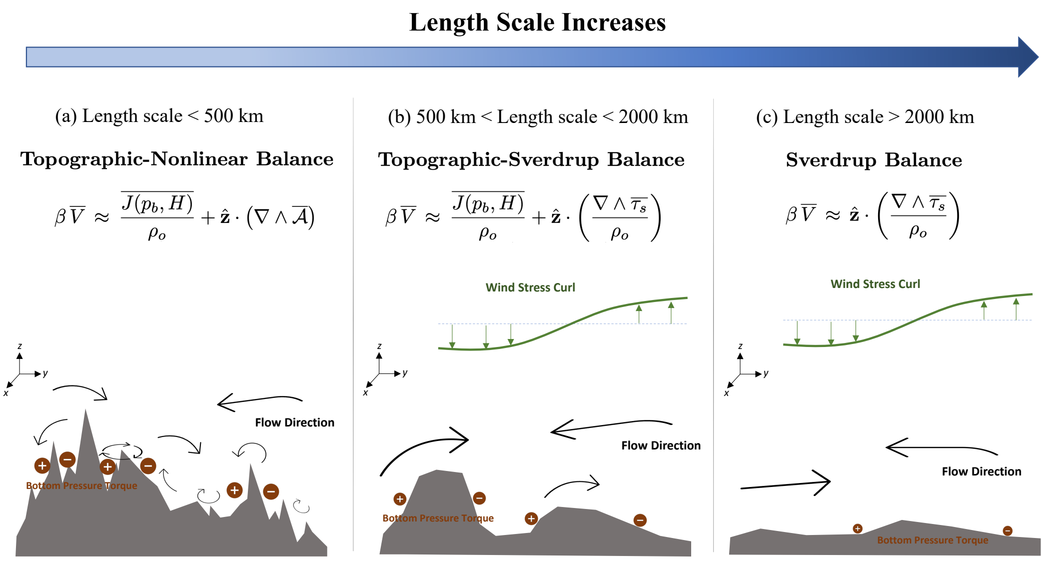

Figure 10. Schematic of primary barotropic vorticity balances and dynamical regimes as a function of length scale in a steady state. Both velocity field (see black arrows) and bottom pressure (brown ± circles) project on all length scales whereas surface wind stress projects only on large length scales. At length scales smaller than 500 km, nonlinear advection and bottom pressure torque control the spatial variability in meridional transport. At length scales greater than 500 km, meridional transport is mainly controlled by bottom pressure torque and surface wind stress curl as the nonlinear advection contribution is insignificant at large length scales.

get terms are analyzed as a function of spatial-filtering scale by employing the coarse-graining technique (Buzzicotti et al., 2023; Storer et al., 2022). Consistent with previous studies (Hughes & De Cuevas, 2001; Sonnewald et al., 2019), the relative magnitudes of different vorticity budget terms display significant regional variability. In general, depth-integrated meridional velocity is balanced by a combination of the surface wind stress curl, bottom pressure torque, and the curl of the nonlinear velocity advection in the barotropic vorticity budget. The relative importance of these terms is examined by performing vorticity analyses in different ocean regions at different filter scales.

We show that Topographic-Svedrup balance, in which βV (meridional gradient of Coriolis parameter $\times$ depth-integrated meridional velocity), bottom pressure torque, and surface wind stress curl are in balance (Holland, 1967), applies to vorticity dynamics in the majority of the global ocean. These three vorticity terms capture more than 70% of the spatial-pattern variability in the barotropic vorticity budget (Figures 3–8); however, it requires significant spatial filtering, and this simplified balance only holds at length scales larger than about 10° (or roughly 1000 km). This result is in agreement with previous studies that employed coarse non-eddy resolving model outputs in their vorticity analyses (Lu & Stammer, 2004; Yeager, 2015). Although bottom pressure torque contribution is significant in all ocean regions that we considered, a simpler Sverdrup balance, in which the depth-integrated meridional transport is driven by surface wind stress curl (Sverdrup, 1947), holds reasonably well in subtropical oceans at length scales greater than 10° (also see Gray & Riser, 2014; Thomas et al., 2014; Wunsch, 2011). On the other hand, at higher latitudes and throughout the Southern Ocean, the contribution of bottom pressure torque for the vorticity balance cannot be neglected, with this importance due to relatively strong deep flows.

In the case of nominal or no coarse-graining (retaining variations on length scales greater than 1° in the present work), bottom pressure torque and the nonlinear advection term dominate the vorticity budget locally (referred to as "Topographic-Nonlinear" balance here) indicating a prominent role of ocean eddies in vorticity balances. We note that bottom pressure torque and nonlinear advection terms compensate against each other (e.g. see Le Corre et al., 2020), and the residual from these two terms is roughly balanced by βV. As we increase the length scale of spatial filtering, the nonlinear advection term largely smooths out, and we find a clear transition from Topographic-Nonlinear balance to Topographic-Sverdrup balance in the local vorticity budget (see Figures 9–10). Hence, the nonlinear advection term contributes to vorticity balances mostly at length scales smaller than 10° (roughly 1000 km), and we offer a scaling argument to explain why it plays a negligible role for larger scale vorticity balances.

By incorporating the coarse-graining method in vorticity budget analysis, we find that the relative magnitudes of vorticity budget terms not only vary regionally but also have a strong length-scale dependence. Although Sverdrup and Topographic-Sverdrup relationships explain the spatial structure of the meridional transport in many places, these relationships only apply to large-scale oceanic flows (larger than about 1000 km). At relatively small length scales, the contribution of eddies and nonlinear advection to vorticity balance tends to be significant. Hence, the interpretations from vorticity analyses can be completely different depending on the extent of spatial filtering.

The present study only considers time-mean vorticity balances and the temporal variability in local vorticity balances has not been analyzed. Preliminary vorticity analyses from seasonal vorticity diagnostics (not shown) closely follow the time-mean results presented in the present work. In temporally varying vorticity diagnostics, we expect similar transitions among different dynamical regimes at different length scales (Figure 9) in barotropic vorticity balances, albeit some regional differences may be present.

Appendix A Vorticity Budget of the Depth-integrated Flow

The governing hydrostatic and Boussinesq ocean primitive velocity equation on a generalized vertical coordinate $r = r(x, y, z, t)$ is given by (Adcroft et al., 2019; Griffies et al., 2020)

$$\frac{\partial \mathbf{u}}{\partial t} + (f + \zeta)\,\hat{\boldsymbol{z}} \wedge \mathbf{u} + w^{(\dot{r})}\frac{\partial \mathbf{u}}{\partial r} = -\left[\frac{\nabla_r p}{\rho_o} + \nabla_r \Phi\right] - \nabla_r K + \mathcal{F} + \frac{\partial_r \tau}{\rho_o}, \tag{A1}$$

where we have

$$\mathbf{v} = \mathbf{u} + \hat{\boldsymbol{z}}\,w = \hat{\boldsymbol{x}}\,u + \hat{\boldsymbol{y}}\,v + \hat{\mathbf{z}}\,w \qquad \text{velocity} \tag{A2}$$

$$\nabla_s = \hat{\boldsymbol{x}}\left[\frac{\partial}{\partial x}\right]_r + \hat{\boldsymbol{y}}\left[\frac{\partial}{\partial y}\right]_r \qquad \text{horizontal gradient on } r\text{-surface} \tag{A3}$$

$$w^{(\dot{r})} = \frac{\partial z}{\partial r}\frac{\mathrm{D}r}{\mathrm{D}t} \qquad \text{dia-surface velocity used for remapping} \tag{A4}$$

$$\zeta = \left[\frac{\partial v}{\partial x}\right]_r - \left[\frac{\partial u}{\partial y}\right]_r \qquad r\text{-coordinate vertical vorticity} \tag{A5}$$

$$-\left[\rho_o^{-1}\nabla_r p + \nabla_r \Phi\right] \qquad \text{horizontal pressure acceleration } (\Phi = gz) \tag{A6}$$

$$K = \frac{u^2 + v^2}{2} \qquad \text{horizontal kinetic energy per mass} \tag{A7}$$

$$\mathcal{F} = \mathcal{F}^{(\text{horz diff})} + \mathcal{F}^{(\text{vert diff})} \qquad \text{horizontal and vertical diffusion} \tag{A8}$$

$$\partial_r \tau = \delta(z-\eta)\boldsymbol{\tau}_{\text{s}} - \delta(z+H)\boldsymbol{\tau}_{\text{b}} \qquad \text{wind stress, } \boldsymbol{\tau}_{\text{s}} \text{ and bottom drag, } \boldsymbol{\tau}_{\text{b}} \tag{A9}$$

$$\delta(z) \qquad \text{Dirac delta with dimensions } L^{-1} \tag{A10}$$

A1 Depth integration and its curl

To derive the vorticity budget of the depth-integrated flow, we first vertically integrate the velocity equation (A1) from the ocean bottom, $z = -H(x,y)$, to the sea surface, $z = \eta(x,y,t)$),

$$\int_{-H}^{\eta} \partial_t \mathbf{u} \, \mathrm{d}z = -f\,\hat{\boldsymbol{z}} \wedge \int_{-H}^{\eta} \mathbf{u} \, \mathrm{d}z - \frac{1}{\rho_o} \int_{-H}^{\eta} \nabla p \, \mathrm{d}z + \frac{\boldsymbol{\tau}_{\text{s}}}{\rho_o} - \frac{\boldsymbol{\tau}_{\text{b}}}{\rho_o} + \int_{-H}^{\eta} \mathbf{a} \, \mathrm{d}z + \int_{-H}^{\eta} \mathbf{b} \, \mathrm{d}z. \tag{A11}$$

Here, $\mathbf{a} = -\zeta\,\hat{\boldsymbol{z}} \wedge \mathbf{u} - \nabla_r K - w^{(\dot{r})}\,\partial_r \mathbf{u}$ and $\mathbf{b} = \mathcal{F}^{(\text{horz diff})}$. By construction, vertical integral of $\mathcal{F}^{(\text{vert diff})}$ over the whole depth vanishes. Since we use the depth-integrated velocity equation to derive the vorticity budget, the mathematical manipulations in the following steps remain the same irrespective of the choice of the vertical coordinate in the velocity equation. Thus, for simplicity, the pressure gradient term is just written as ∇p above, where $\nabla = \hat{\boldsymbol{x}}\,\partial_x + \hat{\boldsymbol{y}}\,\partial_y$ is the horizontal gradient operator on a fixed depth. We now introduce the shorthand notation

$$\mathcal{U}_t = \int_{-H}^{\eta} \partial_t \mathbf{u} \, \mathrm{d}z \quad \text{and} \quad \mathcal{A} = \int_{-H}^{\eta} \mathbf{a} \, \mathrm{d}z \quad \text{and} \quad \mathcal{B} = \int_{-H}^{\eta} \mathbf{b} \, \mathrm{d}z, \tag{A12}$$

and make use of Leibniz's rule on the pressure gradient term to render

$$\mathcal{U}_t = -f\,\hat{\boldsymbol{z}} \wedge \int_{-H}^{\eta} \mathbf{u} \, \mathrm{d}z - \frac{1}{\rho_o} \nabla \left[\int_{-H}^{\eta} p \, \mathrm{d}z \right] + p_{\text{s}}\,\nabla\eta + p_{\text{b}}\,\nabla H + \frac{\boldsymbol{\tau}_{\text{s}}}{\rho_o} - \frac{\boldsymbol{\tau}_{\text{b}}}{\rho_o} + \mathcal{A} + \mathcal{B}. \tag{A13}$$

Here, p_{s} and p_{b} are pressures at the surface and bottom of the ocean, and the terms $p_{\text{s}}\,\nabla\eta$, $p_{\text{b}}\,\nabla H$ are pressure form stresses at the ocean surface and ocean bottom, respectively. We now take the curl of this equation and split the curl of the linear Coriolis term into two terms to obtain

$$\begin{aligned}
\nabla \wedge \mathcal{U}_t \quad &= \quad -\nabla \wedge \left(f\,\hat{\boldsymbol{z}} \wedge \int_{-H}^{\eta} \mathbf{u} \, \mathrm{d}z \right) - \frac{1}{\rho_o} \nabla \wedge \left(\nabla \int_{-H}^{\eta} p \, \mathrm{d}z - p_{\text{s}}\,\nabla\eta - p_{\text{b}}\,\nabla H \right) \\
&\quad + \frac{\nabla \wedge \boldsymbol{\tau}_{\text{s}}}{\rho_o} - \frac{\nabla \wedge \boldsymbol{\tau}_{\text{b}}}{\rho_o} + \nabla \wedge \mathcal{A} + \nabla \wedge \mathcal{B}, \qquad (\text{A14}) \\
\hat{\boldsymbol{z}} \cdot (\nabla \wedge \mathcal{U}_t) \quad &= \quad -\beta \int_{-H}^{\eta} v \, \mathrm{d}z - f\,\nabla \cdot \int_{-H}^{\eta} \mathbf{u} \, \mathrm{d}z + \frac{J(p_{\text{s}}, \eta)}{\rho_o} + \frac{J(p_{\text{b}}, H)}{\rho_o} \\
&\quad + \hat{\boldsymbol{z}} \cdot \left(\frac{\nabla \wedge \boldsymbol{\tau}_{\text{s}}}{\rho_o} - \frac{\nabla \wedge \boldsymbol{\tau}_{\text{b}}}{\rho_o} + \nabla \wedge \mathcal{A} + \nabla \wedge \mathcal{B} \right). \qquad (\text{A15})
\end{aligned}$$

We can further manipulate the second term on the right hand side (RHS) by making use of volume conservation for a vertical column of Boussinesq fluid, which is

$$\nabla \cdot \int_{-H}^{\eta} \mathbf{u} \, \mathrm{d}z = \frac{Q_m}{\rho_o} - \partial_t \eta. \tag{A16}$$

In addition, many climate models impose a uniform pressure at the ocean surface so that $J(p_s, \eta) = 0$. Finally, the vorticity budget for the depth-integrated flow (with some rearranging and writing $\int_{-H}^{\eta} v = V$) can be written as

$$\beta V = \frac{J(p_b, H)}{\rho_o} + \hat{\boldsymbol{z}} \cdot \left(\frac{\nabla \wedge \boldsymbol{\tau}_s}{\rho_o} - \frac{\nabla \wedge \boldsymbol{\tau}_b}{\rho_o} + \nabla \wedge \mathcal{A} + \nabla \wedge \mathcal{B} \right) - f \, \frac{Q_m}{\rho_o} + f \, \partial_t \eta - \hat{\boldsymbol{z}} \cdot (\nabla \wedge \mathcal{U}_t) \, . \tag{A17}$$

A2 Manipulating the nonlinear advection term

$\nabla \wedge \mathcal{A}$ term can be further manipulated to represent it in a simpler form. In a $z-$coordinate model, we can write $\mathbf{a}$ as

$$\begin{aligned} \mathbf{a} &= a_x \, \hat{\boldsymbol{x}} + a_y \, \hat{\boldsymbol{y}} & \text{(A18)} \\ &= -\nabla_3 \cdot (\mathbf{v} u) \;\; \hat{\boldsymbol{x}} - \nabla_3 \cdot (\mathbf{v} v) \;\; \hat{\boldsymbol{y}}, & \text{(A19)} \end{aligned}$$

where $\mathbf{v} = \mathbf{u} + \hat{\boldsymbol{z}} \, w = \hat{\boldsymbol{x}} \, u + \hat{\boldsymbol{y}} \, v + \hat{\mathbf{z}} \, w$ is the velocity and $\nabla_3 = \nabla + \hat{\boldsymbol{z}} \, \partial_z$. We can integrate $\mathbf{a}$ vertically to obtain $\mathcal{A} = \mathcal{A}_x \, \hat{\boldsymbol{x}} + \mathcal{A}_y \, \hat{\boldsymbol{y}}$ (Leibniz's rule is also used),

$$\begin{aligned} \mathcal{A}_x &= a_x = -\int_{-H}^{\eta} \nabla_3 \cdot (\mathbf{v} \, u) \; \mathrm{d}z & \text{(A20)} \\ &= -\int_{-H}^{\eta} \nabla \cdot (\mathbf{u} \, u) \; \mathrm{d}z - [w \, u]^{z=\eta} + [w \, u]^{z=-H} & \text{(A21)} \\ &= -\nabla \cdot \int_{-H}^{\eta} (\mathbf{u} \, u) \; \mathrm{d}z + [\mathbf{u} \, u]^{z=\eta} \cdot \nabla \eta + [\mathbf{u} \, u]^{z=-H} \cdot \nabla H & \\ &\quad - [w \, u]^{z=\eta} + [w \, u]^{z=-H}. & \text{(A22)} \end{aligned}$$

We can further simplify the above equation by using the surface and bottom kinematic boundary conditions,

$$\begin{aligned} \frac{\partial \eta}{\partial t} + \mathbf{u} \cdot \nabla \eta &= w + \frac{Q_m}{\rho_o} \quad \text{at} \quad z = \eta, & \text{(A23)} \\ -\mathbf{u} \cdot \nabla H &= w \quad \text{at} \quad z = -H. & \text{(A24)} \end{aligned}$$

Using equations A22–A24 and following the same steps for A_y, we obtain

$$\begin{aligned} \mathcal{A}_x &= -\nabla \cdot \int_{-H}^{\eta} (\mathbf{u} \, u) \; \mathrm{d}z + \left(\frac{Q_m}{\rho_o} - \frac{\partial \eta}{\partial t} \right) [u]^{z=\eta} & \text{(A25)} \\ \mathcal{A}_y &= -\nabla \cdot \int_{-H}^{\eta} (\mathbf{u} \, v) \; \mathrm{d}z + \left(\frac{Q_m}{\rho_o} - \frac{\partial \eta}{\partial t} \right) [v]^{z=\eta} & \text{(A26)} \end{aligned}$$

Finally, the nonlinear advection term in the barotropic vorticity budget can be written

$$\begin{aligned}\nabla \wedge \mathcal{A} &= -\nabla \wedge \left(\hat{\boldsymbol{x}}\, \nabla \cdot \int_{-H}^{\eta} (\mathbf{u}\, u)\, \mathrm{d}z + \hat{\boldsymbol{y}}\, \nabla \cdot \int_{-H}^{\eta} (\mathbf{u}\, v)\, \mathrm{d}z \right) \\ &\quad + \nabla \wedge \left(\left(\frac{Q_m}{\rho_o} - \frac{\partial \eta}{\partial t} \right) [\mathbf{u}]^{z=\eta} \right), \qquad \text{(A27)} \\ \nabla \wedge \mathcal{A} &= \frac{1}{\rho_o} \nabla \wedge \left(\nabla \cdot \int_{-H}^{\eta} \mathbb{T}^{\text{kinetic}}_{\text{hor}}\, \mathrm{d}z \right) + \nabla \wedge \left(\left(\frac{Q_m}{\rho_o} - \frac{\partial \eta}{\partial t} \right) [\mathbf{u}]^{z=\eta} \right), \qquad \text{(A28)}\end{aligned}$$

where $\mathbb{T}^{\text{kinetic}}_{\text{hor}} = -\rho_o\, \mathbf{u} \otimes \mathbf{u}$ is the horizontal kinetic stress tensor. The second term of the RHS in equation (A28) is generally very small and can be neglected (Figure 2). Thus, the nonlinear advection term is mainly due to $\mathbb{T}^{\text{kinetic}}_{\text{hor}}$.

Appendix B Diagnosing Vorticity Budget Terms in MOM6

MOM6 is equipped with online diagnostics sufficient for an offline computation of individual terms in the vorticity equations (A17). We do so by making use of the online depth-integrated velocity budget diagnostics in MOM6. We then take the curl of these diagnostics to obtain the corresponding vorticity budget terms. Actual names of depth-integrated momentum diagnostics and the relevant calculations are shown in Table B1. A more detailed description of velocity and vorticity budget diagnostic calculations in MOM6 is available at Khatri et al. (2023).

B1 Remapping contribution

In MOM6, the layer-wise discrete zonal and meridional velocity budgets can be diagnosed according to

$$\begin{aligned}\texttt{dudt} &= \texttt{CAu} + \texttt{PFu} + \texttt{u\_BT\_accel} + \texttt{du\_dt\_visc} + \texttt{diffu} + \texttt{remapping(u)}, \qquad \text{(B1)} \\ \texttt{dvdt} &= \texttt{CAv} + \texttt{PFv} + \texttt{v\_BT\_accel} + \texttt{dv\_dt\_visc} + \texttt{diffv} + \texttt{remapping(v)}. \qquad \text{(B2)}\end{aligned}$$

Except for the last term on the RHS in equations (B1-B2), the rest of the terms are names of the MOM6 diagnostics corresponding to terms in equation (A1). The remapping terms correspond to $w^{(\dot{s})}\, \partial_z \mathbf{u}$, which are diagnosed offline as a residual in the velocity budget as

$$\begin{aligned}\texttt{remapping(u)} &= \texttt{dudt} - \texttt{CAu} - \texttt{PFu} - \texttt{u\_BT\_accel} - \texttt{du\_dt\_visc} - \texttt{diffu} \qquad \text{(B3)} \\ \texttt{remapping(v)} &= \texttt{dvdt} - \texttt{CAv} - \texttt{PFv} - \texttt{v\_BT\_accel} - \texttt{dv\_dt\_visc} - \texttt{diffv}. \qquad \text{(B4)}\end{aligned}$$

Term	Relevant Diagnostic Calculations
V	$\texttt{vmo\_2d}/(\rho_o \Delta x)$, where Δx is the zonal grid spacing and $\rho_o = 1035$ kg m^{-3}
$J(p_\mathrm{b}, H)$	see section B2
$\hat{\boldsymbol{z}} \cdot (\nabla \wedge \boldsymbol{\tau}_\mathrm{s})$	$\partial_x\, [\texttt{tauy}] - \partial_y\, [\texttt{taux}]$
$\hat{\boldsymbol{z}} \cdot (\nabla \wedge \boldsymbol{\tau}_\mathrm{b})$	$\partial_x\, [\texttt{tauy\_bot}] - \partial_y\, [\texttt{taux\_bot}]$
$\hat{\boldsymbol{z}} \cdot (\nabla \wedge \mathcal{A})$	$\partial_x\, [\texttt{intz\_rvxu\_2d} + \texttt{intz\_gKEv\_2d}] - \partial_y\, [\texttt{intz\_rvxv\_2d} + \texttt{intz\_gKEu\_2d}]$ + vertical remap contribution
$\hat{\boldsymbol{z}} \cdot (\nabla \wedge \mathcal{B})$	$\partial_x\, [\texttt{intz\_diffv\_2d}] - \partial_y\, [\texttt{intz\_diffu\_2d}]$
Q_m	$\texttt{wfo}$ or $\texttt{PRCmE}$
$\partial_t \eta$	$\texttt{wfo}/\rho_o - \partial_x\, [\texttt{umo\_2d}/(\rho_o \Delta y)] - \partial_y\, [\texttt{vmo\_2d}/(\rho_o \Delta x)]$ (following equation (A16))
$\hat{\boldsymbol{z}} \cdot (\nabla \wedge \mathcal{U}_t)$	$\partial_x\, [D \times \texttt{hf\_dvdt\_2d}] - \partial_y\, [D \times \texttt{hf\_dudt\_2d}]$

Table B1. Method for the computations of vorticity budget terms using depth-integrated momentum budget diagnostics ($D = H + \eta$ is the full depth of the ocean) in MOM6. The contribution from remapping in $\nabla \wedge \mathcal{A}$ can be computed as discussed in section B1.

To compute the contribution of the remapping terms in the vorticity budget, we calculate the curl of the depth-integrated remapping terms diagnosed as residuals from the depth-integrated velocity budget diagnostics.

B2 Bottom pressure torque calculation

In the present analysis, bottom pressure torque is diagnosed as the following

$$\frac{J(p_\mathrm{b}, H)}{\rho_o} = \hat{\boldsymbol{z}} \cdot \left(-\nabla \wedge \left[\frac{1}{\rho_o} \int_{-H}^{\eta} \nabla p \, \mathrm{d}z \right] - \nabla \wedge \left[f \hat{\mathbf{z}} \wedge \int_{-H}^{\eta} \mathbf{u} \, \mathrm{d}z \right] \right) + \beta V + f \frac{Q_m}{\rho_o} - f \partial_t \eta, \quad \text{(B5)}$$

which then leads to the following diagnostic equation

$$\begin{aligned} \frac{J(p_\mathrm{b}, H)}{\rho_o} &= \partial_x\, [\texttt{intz\_PFv\_2d} + \texttt{intz\_v\_BT\_accel\_2d}] - \partial_y\, [\texttt{intz\_PFu\_2d} + \texttt{intz\_u\_BT\_accel\_2d}] \\ &+ \partial_x\, [\texttt{intz\_CAv\_2d} - \texttt{intz\_rvxu\_2d} - \texttt{intz\_gKEv\_2d}] \\ &- \partial_y\, [\texttt{intz\_CAu\_2d} - \texttt{intz\_rvxv\_2d} - \texttt{intz\_gKEu\_2d}] \\ &+ \frac{\beta}{\rho_o \Delta x} \times \texttt{vmo\_2d} + \frac{f}{\rho_o} \times \texttt{wfo} - f \partial_t \eta. \end{aligned} \quad \text{(B6)}$$

From the development in equations A14-A16, sum of the last four terms on the RHS in equation B5 vanishes.

$$\hat{\boldsymbol{z}} \cdot \left(\nabla \wedge \left[f \hat{\mathbf{z}} \wedge \int_{-H}^{\eta} \mathbf{u} \, \mathrm{d}z \right] \right) = \beta V + f \frac{Q_m}{\rho_o} - f \partial_t \eta \tag{B7}$$

Hence, the analytical expression B5 basically computes the curl of the depth-integrated pressure gradient terms, which is bottom pressure torque.

However, the analytical result in equation B7 need not hold in an ocean model, which solves for velocity on a discretized grid. Theoretically, the zonal and meridional gradients in the curl operations over planetary vorticity advection terms (LHS in equation B7) largely cancel out and the small residual is equal to βV (plus small contributions from nonzero Q_m and $\partial_t \eta$). A similar cancellation is expected in the curl of depth-integrated pressure gradient terms and the small residual is the measure of bottom pressure torque. However, on the MOM6 grid, the cancellation between the zonal and meridional gradients in $\nabla \wedge \left[f \hat{\mathbf{z}} \wedge \int_{-H}^{\eta} \mathbf{u} \, \mathrm{d}z \right]$ does not occur as expected and the residual is at least two orders of magnitudes larger than βV (compare Figures B1a and B1b). Similarly, $-\nabla \wedge \left[\frac{1}{\rho_o} \int_{-H}^{\eta} \nabla p \, \mathrm{d}z \right]$ suffers from unrealistic large residuals (Figure B1d). These large residuals are just numerical errors due to model discretization.

Styles et al. (2022) showed that vorticity budget terms suffer from spurious signals in ocean models based on the C-grid (Mesinger & Arakawa, 1976). These spurious signals arise due to the handling of Coriolis advection and representation of bathymetry in energy and enstrophy conserving schemes on a discrete C-grid (Arakawa & Lamb, 1981). As a result, a C-grid model does not satisfy discrete versions of the divergence theorem and Leibniz's rule, which are used in equation A13, leading to spurious forces in the vorticity budget. MOM6 is discretized using a C-grid and employs a vertical Lagrangian-remap method on a hybrid z^*-isopycnal vertical coordinate to simulate the ocean state (Adcroft et al., 2019; Griffies et al., 2020). Hence, vorticity budget terms diagnosed in MOM6 model are expected to suffer from spurious forces as suggested by Styles et al. (2022).

It turns out that numerical errors in $-\nabla \wedge \left[f \hat{\mathbf{z}} \wedge \int_{-H}^{\eta} \mathbf{u} \, \mathrm{d}z \right]$ and $-\nabla \wedge \left[\frac{1}{\rho_o} \int_{-H}^{\eta} \nabla p \, \mathrm{d}z \right]$ are opposite in sign (see Figures B1a, B1d) and these numerical errors almost disappear in the summation of curls of depth-integrated Coriolis advection and pressure gradient terms. Hence, we employ equation B6 to diagnose bottom pressure torque from the model as this approach results in realistic magnitudes and spatial structure of bottom pressure

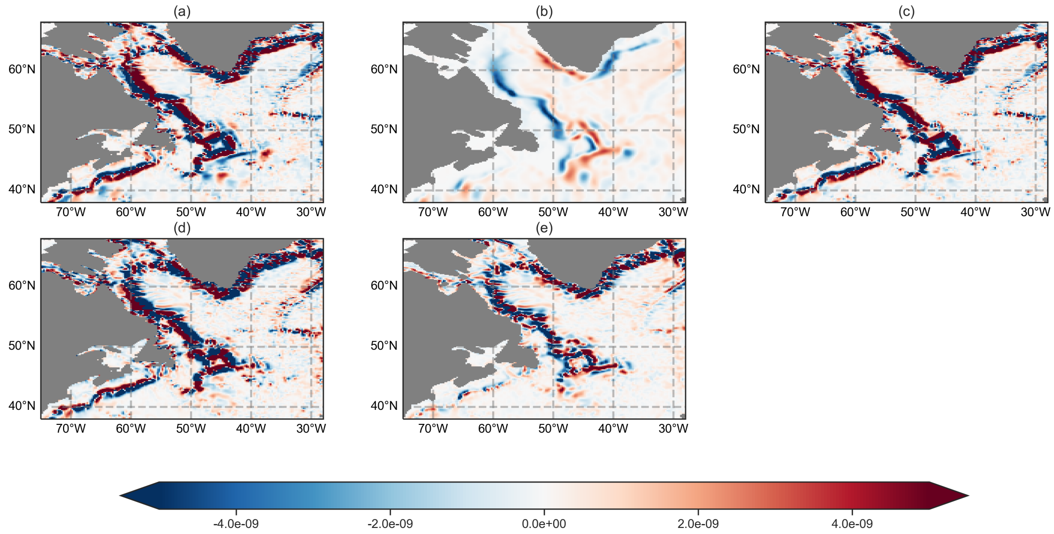

Figure B1. Time-mean (1958–2017) of (a) Vertical component of the curl of depth-integrated planetary vorticity advection, $-\nabla \wedge \left[f\hat{\mathbf{z}} \wedge \int_{-H}^{\eta} \mathbf{u}\,\mathrm{d}z\right]$, in model diagnostics (terms in second and third lines on the RHS in equation B6) (b) $\beta V + f Q_m/\rho_o - f\partial_t\eta$ (c) sum of fields shown in panels a and b (d) Vertical component of the the curl of depth-integrated pressure gradient, $-\nabla \wedge \left[\frac{1}{\rho_o}\int_{-H}^{\eta} \nabla p\,\mathrm{d}z\right]$, in model diagnostics (terms in the first line on the RHS in equation B6) (e) sum of fields shown in panels c and d to compute bottom pressure torque. No coarse-graining (or regridding) was applied and the plotted diagnostics are on the actual model grid. However, for a better visualization, plotted diagnostics were smoothed by averaging over neighboring four grid points to remove grid-scale noise (used GCM-Filters package Loose et al., 2022).

torque. For example, compare Figure B1e with Figure 7b in Le Corre et al. (2020), who used a terrain following vertical coordinate model. Our diagnostic approach essentially assumes that numerical errors in $-\nabla \wedge \left[f\hat{\mathbf{z}} \wedge \int_{-H}^{\eta} \mathbf{u}\,\mathrm{d}z\right]$ and $-\nabla \wedge \left[\frac{1}{\rho_o}\int_{-H}^{\eta} \nabla p\,\mathrm{d}z\right]$ are exactly opposite in sign, which need not be true in general. Numerical errors may also be present in nonlinear advection, bottom stress, and horizontal friction in the barotropic vorticity budget. However, pressure gradient and Coriolis advection in velocity equations are at least two orders of magnitude larger than the rest of the terms (Figure B2). Thus, it is safe to assume that numerical errors are contained in pressure gradient and Coriolis advection, and the diagnostic approach (equation B6) works well in practice.

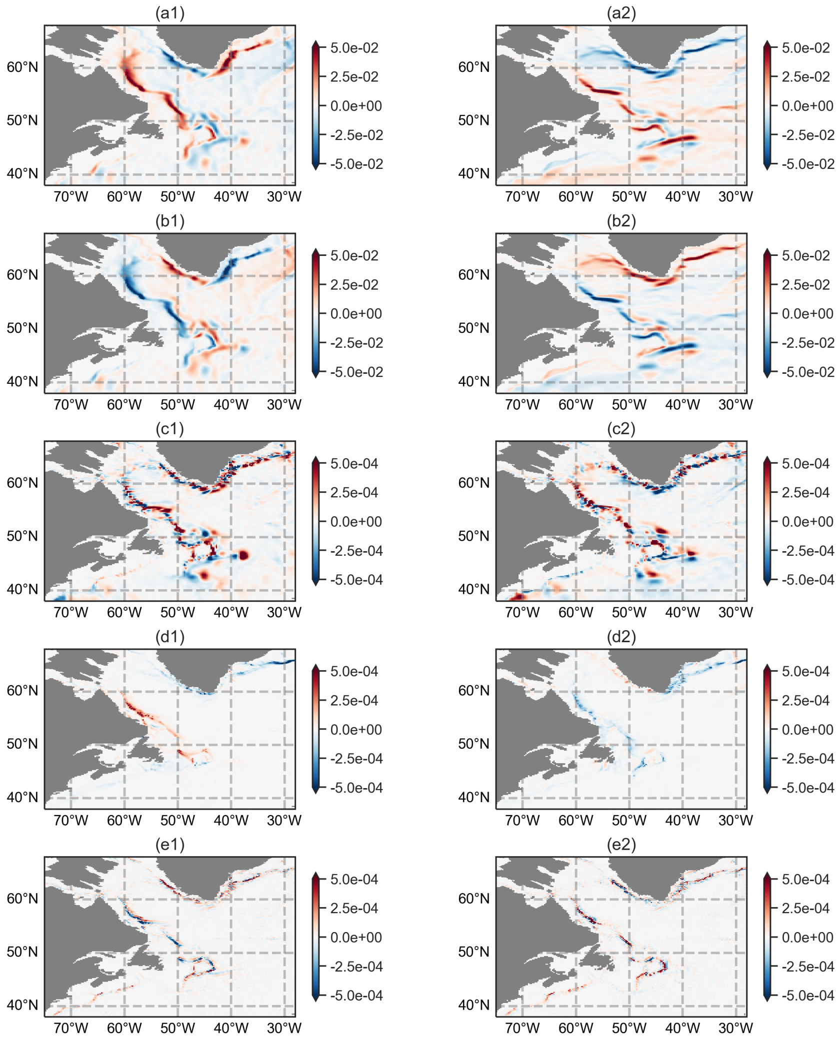

Figure B2. Time-mean (1958–2017) model diagnostics for (a) Depth-integrated pressure gradient term, $-\frac{1}{\rho_o}\int_{-H}^{\eta} \nabla p \, \mathrm{d}z$, (b) Depth-integrated Coriolis advection, $-f\hat{\mathbf{z}} \wedge \int_{-H}^{\eta} \mathbf{u} \, \mathrm{d}z$, (c) Depth-integrated nonlienar advection, $\mathcal{A}$, (d) Bottom friction term, $-\boldsymbol{\tau}_{\mathrm{b}}/\rho_o$, (e) Depth-integrated horizontal diffusion term, $\mathcal{B}$. Left and right panels are for the zonal and meridional velocity diagnostics, respectively.

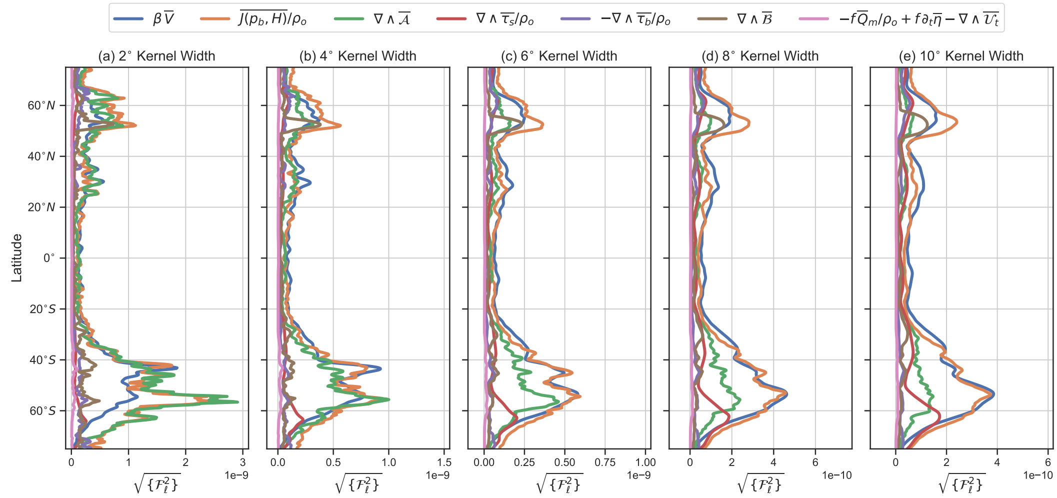

Figure C1. Latitude vs root-mean-square magnitudes, $\sqrt{\{F_\ell^2\}}$, of vorticity budget terms as a function of the coarse-graining filter scale. Note that $\hat{\boldsymbol{z}}\cdot$ is omitted in the legends.

Appendix C Coarse-graining and Vorticity Budget Magnitudes

To assess the impact of coarse-graining on the actual magnitudes of vorticity budget terms, the zonally-averaged profiles of $\sqrt{\{F_\ell^2\}}$ are examined. As seen in Figure C1, root-mean-square magnitudes of the vorticity budget terms are largest in the Southern Ocean (between 40°S and 60°S) followed by oceanic regions at 50°N–70°N latitude bands. $\sqrt{\{F_\ell^2\}}$ values of coarse-grained fields for 2° filter scale are larger by a factor of ten than $\sqrt{\{F_\ell^2\}}$ values for 10° filter scale. In the zonal average, βV, bottom pressure torque, and nonlinear advection term are of the largest magnitudes. With increasing the coarse-graining filter scale, $\nabla\wedge\mathcal{A}$ term becomes much smaller and βV is mainly balanced by bottom pressure torque.

Appendix D Sensitivity of Vorticity Balances to the Filtering Method

To test the dependence of vorticity balances on the shape of filter kernel and filtering algorithm, we spatially filter the vorticity budget terms with a Gaussian kernel using GCM-Filters package (Loose et al., 2022), which employs a diffusion-based filtering scheme (Grooms et al., 2021), and repeat the analysis shown in section 3.1. In contrast to the fixed-kernel approach that we used in coarse-graining, GCM-Filters modifies the shape of the Gaussian kernel near land-sea boundaries (Grooms et al., 2021).

Nevertheless, the spatial maps of filtered vorticity terms in Figure D1 look similar to maps shown in Figure 3 and the overall conclusions about vorticity balances remain the same.

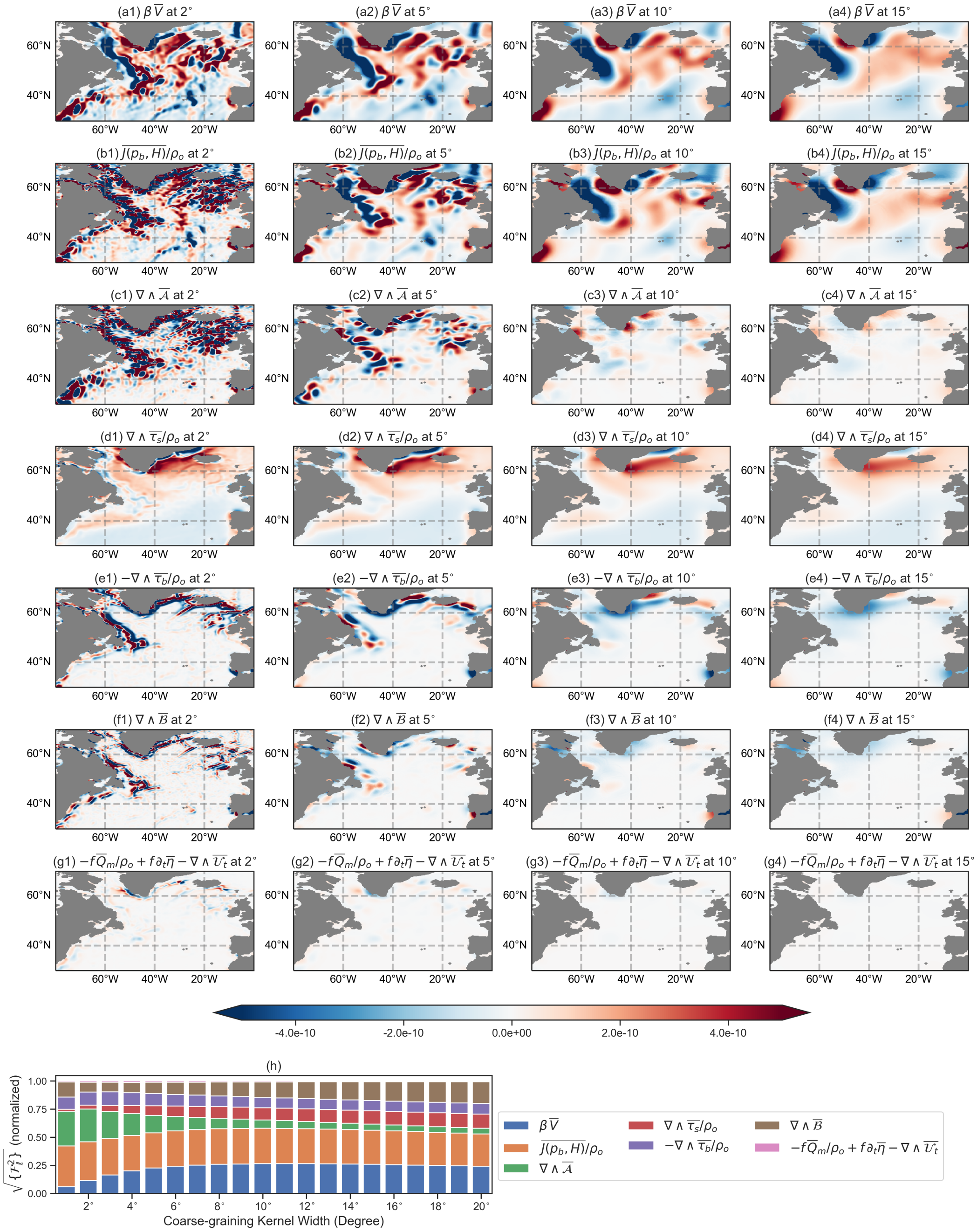

Figure D1. Vorticity budget analysis for the North Atlantic Ocean (a-g) Time-mean (1958–2017, indicated with overbars) spatial maps of filtered barotropic vorticity budget terms (used GCM-Filters package, units are in m s^{-2}) as a function of filter scale; (h-i) Normalized magnitudes of the root-mean-square budget terms (see equation 6) at different filter scales (in degree). $\sqrt{\{F_\ell^2\}}$ is computed for the region bounded between 30°N–70°N and 80°W–0°W. Note that $\hat{\boldsymbol{z}}\cdot$ is omitted in panel titles and legends.

Acknowledgments

The authors thank Alistair Adcroft and Robert Hallberg for help with the implementation of depth-integrated momentum budget diagnostics in MOM6. Discussions with Chris Hughes were very helpful in this work, and we thank Graeme MacGilchrist and Wenda Zhang for comments on a draft of this manuscript. HK acknowledges the support from National Oceanic and Atmospheric Administration (NOAA) grant NA18OAR4320123 and Natural Environment Research Council (NERC) grant NE/T013494/1. MB acknowledges the support from the European Research Council (ERC) under the European Union's Horizon 2020 research and innovation programme (Grant Agreement No. 882340). HA and BS acknowledge support from US NASA grant 80NSSC18K0772 and US NSF grants OCE-2123496, PHY-2020249.

Open Research

FlowSieve filtering package (Storer & Aluie, 2023) used in the analysis of this paper is available at `https://github.com/husseinaluie/FlowSieve`. Post-processed data and Python scripts used to produce the figures are available at Khatri et al. (2023).

References

Adcroft, A., Anderson, W., Balaji, V., Blanton, C., Bushuk, M., Dufour, C. O., ... others (2019). The gfdl global ocean and sea ice model om4. 0: Model description and simulation features. *Journal of Advances in Modeling Earth Systems*, *11*(10), 3167–3211. doi: 10.1029/2019MS001726

Aluie, H. (2019). Convolutions on the sphere: Commutation with differential operators. *GEM-International Journal on Geomathematics*, *10*(1), 1–31. doi: 10.1007/s13137-019-0123-9

Aluie, H., Hecht, M., & Vallis, G. K. (2018). Mapping the energy cascade in the North Atlantic Ocean: The coarse-graining approach. *Journal of Physical Oceanography*, *48*(2), 225–244. doi: 10.1175/JPO-D-17-0100.1

Arakawa, A., & Lamb, V. R. (1981). A potential enstrophy and energy conserving scheme for the shallow water equations. *Monthly Weather Review*, *109*(1), 18–36. doi: 10.1175/1520-0493(1981)109$⟨$0018$:$APEAEC$⟩$2.0.CO$;$2

Buzzicotti, M., Storer, B. A., Khatri, H., Griffies, S. M., & Aluie, H. (2023). Spatio-temporal coarse-graining decomposition of the global ocean geostrophic kinetic energy. *arXiv preprint arXiv:2106.04157v2*. doi: 10.48550/arXiv.2106.04157

Chelton, D. B., Schlax, M. G., & Samelson, R. M. (2011). Global observations of nonlinear mesoscale eddies. *Progress in oceanography*, *91*(2), 167–216. doi: 10.1016/j.pocean.2011.01.002

Chelton, D. B., Schlax, M. G., Samelson, R. M., & de Szoeke, R. A. (2007). Global observations of large oceanic eddies. *Geophysical Research Letters*, *34*(15). doi: 10.1029/2007GL030812

Eden, C. (2007). Eddy length scales in the North Atlantic Ocean. *Journal of Geophysical Research: Oceans*, *112*(C6). doi: 10.1029/2006JC003901

Gray, A. R., & Riser, S. C. (2014). A global analysis of Sverdrup balance using absolute geostrophic velocities from Argo. *Journal of Physical Oceanography*, *44*(4), 1213–1229. doi: 10.1175/JPO-D-12-0206.1

Griffies, S. M., Adcroft, A., & Hallberg, R. W. (2020). A primer on the vertical Lagrangian-remap method in ocean models based on finite volume generalized vertical coordinates. *Journal of Advances in Modeling Earth Systems*, *12*(10), e2019MS001954. doi: 10.1029/2019MS001954

Griffies, S. M., Danabasoglu, G., Durack, P. J., Adcroft, A. J., Balaji, V., Böning, C. W., ... Yeager, S. (2016). Omip contribution to cmip6: Experimental and diagnostic protocol for the physical component of the Ocean Model Intercomparison Project. *Geoscientific Model Development*, *9*, 3231–3296. doi: 10.5194/gmd-9-3231-2016

Grooms, I., Loose, N., Abernathey, R., Steinberg, J., Bachman, S. D., Marques, G., ... Yankovsky, E. (2021). Diffusion-based smoothers for spatial filtering of gridded geophysical data. *Journal of Advances in Modeling Earth Systems*, *13*(9), e2021MS002552. doi: 10.1029/2021MS002552

Gula, J., Molemaker, M. J., & McWilliams, J. C. (2015). Gulf Stream dynamics along the southeastern US seaboard. *Journal of Physical Oceanography*, *45*(3), 690–715. doi: 10.1175/JPO-D-14-0154.1

Holland, W. R. (1967). On the wind-driven circulation in an ocean with bottom topography. *Tellus*, *19*(4), 582–600. doi: 10.3402/tellusa.v19i4.9825

Holland, W. R. (1973). Baroclinic and topographic influences on the transport in western boundary currents. *Geophysical Fluid Dynamics*, *4*(3), 187–210. doi: 10.1080/03091927208236095

Hughes, C. W. (2000). A theoretical reason to expect inviscid western boundary currents in realistic oceans. *Ocean Modelling*, *2*(1-2), 73–83. doi: 10.1016/S1463-5003(00)00011-1

Hughes, C. W. (2005). Nonlinear vorticity balance of the Antarctic Circumpolar Current. *Journal of Geophysical Research: Oceans*, *110*(C11). doi: 10.1029/2004JC002753

Hughes, C. W., & De Cuevas, B. A. (2001). Why western boundary currents in realistic oceans are inviscid: A link between form stress and bottom pressure torques. *Journal of Physical Oceanography*, *31*(10), 2871–2885. doi: 10.1175/1520-0485(2001)031⟨2871:WWBCIR⟩2.0.CO;2

Jackson, L., Hughes, C. W., & Williams, R. G. (2006). Topographic control of basin and channel flows: The role of bottom pressure torques and friction. *Journal of physical oceanography*, *36*(9), 1786–1805. doi: 10.1175/JPO2936.1

Khatri, H., Griffies, S. M., Storer, B. A., Buzzicotti, M., Aluie, H., Sonnewald, M., … Shao, A. (2023). *Barotropic vorticity budget analysis in a global ocean simulation.* Zenodo. doi: 10.5281/zenodo.7920588

Kundu, P., Cohen, I., & Dowling, D. (2016). *Fluid mechanics.* Academic Press. (921 + xxiv pp)

Le Bras, I. A.-A., Sonnewald, M., & Toole, J. M. (2019). A barotropic vorticity budget for the subtropical North Atlantic based on observations. *Journal of Physical Oceanography*, *49*(11), 2781–2797. doi: 10.1175/JPO-D-19-0111.1

Le Corre, M., Gula, J., & Treguier, A.-M. (2020). Barotropic vorticity balance of the North Atlantic subpolar gyre in an eddy-resolving model. *Ocean Science*, *16*(2), 451–468. doi: 10.5194/os-16-451-2020

Loose, N., Abernathey, R., Grooms, I., Busecke, J., Guillaumin, A., Yankovsky, E., … others (2022). Gcm-filters: A python package for diffusion-based spatial filtering of gridded data. *Journal of Open Source Software*, *7*(70), 3947. doi: 10.21105/joss.03947

Lu, Y., & Stammer, D. (2004). Vorticity balance in coarse-resolution global ocean simulations. *Journal of physical oceanography*, *34*(3), 605–622. doi: 10.1175/2504.1

Mertz, G., & Wright, D. G. (1992). Interpretations of the JEBAR term. *Journal of Physical Oceanography*, *22*(3), 301–305. doi: 10.1175/1520-0485(1992)

022⟨0301:IOTJT⟩2.0.CO;2

Mesinger, F., & Arakawa, A. (1976). Numerical methods used in atmospheric models, volume 1. *Global Atmospheric Research Program World Meteorological Organization.*

Munk, W. H. (1950). On the wind-driven ocean circulation. *Journal of Atmospheric Sciences*, *7*(2), 80–93. doi: 10.1175/1520-0469(1950)007⟨0080:OTWDOC⟩2.0.CO;2

Palóczy, A., McClean, J. L., Gille, S. T., & Wang, H. (2020). The large-scale vorticity balance of the Antarctic continental margin in a fine-resolution global simulation. *Journal of Physical Oceanography*, *50*(8), 2173–2188. doi: 10.1175/JPO-D-19-0307.1

Rai, S., Hecht, M., Maltrud, M., & Aluie, H. (2021). Scale of oceanic eddy killing by wind from global satellite observations. *Science Advances*, *7*(28), eabf4920. doi: 10.1126/sciadv.abf4920

Rintoul, S. R. (2018). The global influence of localized dynamics in the Southern Ocean. *Nature*, *558*, 209–218. doi: 10.1038/s41586-018-0182-3

Rintoul, S. R., Hughes, C. W., & Olbers, D. (2001). The Antarctic circumpolar current system. In *International geophysics* (Vol. 77, pp. 271–XXXVI). Elsevier. doi: 10.1016/S0074-6142(01)80124-8

Rintoul, S. R., & Naveira Garabato, A. C. (2013). Dynamics of the Southern Ocean circulation. In G. Siedler, S. M. Griffies, J. Gould, & J. Church (Eds.), *Ocean circulation and climate, 2nd edition: A 21st century perspective* (Vol. 103, pp. 471–492). Academic Press.

Schoonover, J., Dewar, W., Wienders, N., Gula, J., McWilliams, J. C., Molemaker, M. J., … Yeager, S. (2016). North atlantic barotropic vorticity balances in numerical models. *Journal of Physical Oceanography*, *46*(1), 289–303. doi: 10.1175/JPO-D-15-0133.1

Sonnewald, M., & Lguensat, R. (2021). Revealing the impact of global heating on North Atlantic circulation using transparent machine learning. *Journal of Advances in Modeling Earth Systems*, *13*(8), e2021MS002496. doi: 10.1029/2021MS002496

Sonnewald, M., Wunsch, C., & Heimbach, P. (2019). Unsupervised learning reveals geography of global ocean dynamical regions. *Earth and Space Science*, *6*(5), 784–794. doi: 10.1029/2018EA000519

Stewart, A. L., McWilliams, J. C., & Solodoch, A. (2021). On the role of bottom pressure torques in wind-driven gyres. *Journal of Physical Oceanography*, *51*(5), 1441–1464. doi: 10.1175/JPO-D-20-0147.1

Stommel, H. (1948). The westward intensification of wind-driven ocean currents. *Eos, Transactions American Geophysical Union*, *29*(2), 202–206.

Storer, B. A., & Aluie, H. (2023). FlowSieve: A Coarse-Graining utility for geophysical flows on the sphere. *Journal of Open Source Software*, *8*(84), 4277. Retrieved from `https://doi.org/10.21105/joss.04277` doi: 10.21105/joss.04277

Storer, B. A., Buzzicotti, M., Khatri, H., Griffies, S. M., & Aluie, H. (2022). Global energy spectrum of the general oceanic circulation. *Nature Communications*, *13*(1), 1–9. doi: 10.1038/s41467-022-33031-3

Styles, A. F., Bell, M. J., Marshall, D. P., & Storkey, D. (2022). Spurious forces can dominate the vorticity budget of ocean gyres on the c-grid. *Journal of Advances in Modeling Earth Systems*, e2021MS002884. doi: 10.1029/2021MS002884

Sverdrup, H. U. (1947). Wind-driven currents in a baroclinic ocean; with application to the equatorial currents of the eastern pacific. *Proceedings of the National Academy of Sciences*, *33*(11), 318–326. doi: 10.1073/pnas.33.11.318

Thomas, M. D., De Boer, A. M., Johnson, H. L., & Stevens, D. P. (2014). Spatial and temporal scales of Sverdrup balance. *Journal of Physical Oceanography*, *44*(10), 2644–2660. doi: 10.1175/JPO-D-13-0192.1

Tsujino, H., Urakawa, S., Griffies, S., Danabasoglu, G., Adcroft, A., Amaral, A., ... Yu, Z. (2020). Evaluation of global ocean-sea-ice model simulations based on the experimental protocols of the Ocean Model Intercomparison Project phase 2 (OMIP-2). *Geoscientific Model Development*, *13*, 3643–3708. doi: 10.5194/gmd-13-3643-2020

Tsujino, H., Urakawa, S., Nakano, H., Small, R., Kim, W., Yeager, S., ... Yamazaki, D. (2018). JRA-55 based surface dataset for driving ocean-sea-ice models (JRA55-do). *Ocean Modelling*, *130*, 79–139. doi: 10.1016/j.ocemod.2018.07.002

Waldman, R., & Giordani, H. (2023). Ocean barotropic vorticity balances: theory and application to numerical models. *Journal of Advances in Modeling Earth Systems*, *15*(4), e2022MS003276. doi: 10.1029/2022MS003276

Wunsch, C. (2011). The decadal mean ocean circulation and Sverdrup balance. *Journal of Marine Research*, *69*(2-3), 417–434. doi: 10.1357/002224011798765303

Yeager, S. (2015). Topographic coupling of the Atlantic overturning and gyre circulations. *Journal of Physical Oceanography*, *45*(5), 1258–1284. doi: 10.1175/JPO-D-14-0100.1